HELSINKI UNIVERSITY OF TECHNOLOGY
Faculty of Electronics, Communications and Automation

Antti Karilainen

THIN-SHEET ANTENNAS BASED ON NETWORKS OF LOADED TRANSMISSION LINES

Thesis submitted for examination for the degree of Master of Science in Technology

Espoo 19.5.2008

Thesis supervisor:

Prof. Sergei Tretyakov

Thesis instructor:

M.Sc.(Tech.) Pekka Alitalo

TEKNILLINEN KORKEAKOULU

DIPLOMITYÖN TIIVISTELMÄ

Tekijä: Antti Karilainen

Työn nimi: Ohuet kuormitettuihin siirtojohtoverkkoihin perustuvat antennit

Päivämäärä: 19.5.2008 Kieli: Englanti Sivumäärä: 10+72

Osasto: Elektroniikka ja sähkötekniikka

Professuuri: Radiotekniikka Koodi: S-26

Valvoja: Prof. Sergei Tretyakov

Ohjaaja: DI Pekka Alitalo

Tässä diplomityössä tutkittiin kaksiulotteisen kuormitettuihin siirojohtoverkkoihin perustuvan antennin toteutusta ilman monimutkaista syöttöverkkoa. Päämääränä oli tutkia, onko mahdollista saada aikaan tasomainen, tasaisesti herätetty rakenne, jolla on sama vaihe jokaisessa pisteessä. Tällöin rakenne toimii rintamasäteilijänä, ja pääkeilan leveyttä voitaisiin muuttaa rakenteen kokoa muuttamalla. Antenni suunniteltiin ensin yksiulotteisen periodisen siirtojohtoverkon ja dispersion avulla halutuksi. Toimintaa tutkittiin analyyttisten laskelmien sekä elementtimenetelmäohjelmisto HFSS:n avulla. Tämän jälkeen suunniteltiin vastaava antenni tasossa käyttäen samaa periaatetta. Tämän kaksiulotteisen $N \times N$ yksikkösolun kokoisen antennin syöttöä tutkittiin N:llä syötöllä yhdeltä reunalta sekä yhdellä syötöllä kulmasta. Huomattiin, että kulmasta syötetty antenni toimii rintamasäteilijänä siinä missä yhdeltäkin reunalta syötetty kaksiulotteinen rakenne. Aallon etenemiselle johdettiin piirimalli äärellisessä siirtojohtoverkossa aksiaalisessa ja diagonaalisessa suunnassa. Kulmasta syötetyn rakenteen antenni-impedanssissa ja sovituksessa on kuitenkin suuri ero yksiulotteiseen rakenteeseen verrattuna, mikä estää sen laajakaistaisen käytön. Tämä johtui siirtojohtoverkkoantennin reunojen sovitusvastuksista, joita käytettiin rajaamaan verkko äärelliseen kokoon. Yksinkertainen sovituspiiri suunniteltiin esimerkkiantenniin rintamasäteilytaajuudella $f_0 = 2.38$ GHz, mikä johti 2,7 prosentin taajuuskaistaan.

Avainsanat: siirtojohtoverkko, vuotoaaltoantenni (vuotavan aallon antenni), taajuuspyyhkäisevä antenni, tasapainoitettu dispersio

HELSINKI UNIVERSITY OF TECHNOLOGY

ABSTRACT OF THE MASTER'S THESIS

Author: Antti Karilainen

Title: Thin-Sheet Antennas Based on Networks of Loaded Transmission Lines

Date: 19.5.2008 Language: English Number of pages: 10+72

Department: Electronics and Electrical Engineering

Professorship: Radio technology Code: S-26

Supervisor: Prof. Sergei Tretyakov

Instructor: M.Sc.(Tech.) Pekka Alitalo

Loaded transmission-line network (TLN) antennas without complex feed networks were studied in this master's thesis. The goal of the study was to determine if it was possible to design a uniformly excited structure with the same phase at every point. This would lead to a broadside antenna, and the beam width of the main beam could be adjusted by changing the size of the TLN. The antenna was first designed with the help of a one-dimensional periodic TLN and dispersion to have the wanted properties. Functionality was inspected with analytical calculations and HFSS full-wave software. After this, a planar antenna with similar properties was designed using the same principles. The feeding of this two-dimensional $N \times N$ TLN structure was studied with N feeds at one edge and one feed at the corner. It was noted that the corned-fed antenna works as a broadside antenna similarly to the edge-fed antenna with multiple feeds, thus removing the need for a complex feeding network. A circuit model for the finite TLN with propagation in axial and diagonal directions was derived. There was, however, a noticeable difference in the antenna impedance of the planar antenna compared to the one-dimensional structure, which prevents the broadband use of the designed antenna. This was caused by the resistive edge-terminations which had to be used to limit the TLN to a finite size. A simple matching circuit was designed for an example antenna at the broadside-radiation frequency $f_0 = 2.38$ GHz, that lead to 2.7 % bandwidth.

Keywords: transmission-line network, leaky-wave antenna, frequency-scanning antenna, balanced dispersion

Preface

This work has been done at the Radio Laboratory (2007) and at the Department of Radio Science and Engineering (2008) of Helsinki University of Technology.

I would like to give my thanks to my supervisor Professor Sergei Tretyakov for this position to work in this rather independent and very challenging academic research topic. I have learned that science is made in surprisingly small steps, but the steps are still very gratifying! Much praise must be also directed to my instructor M.Sc.(Tech.) Pekka Alitalo, not forgetting other work colleagues: Jari Holopainen, Liisi Jylhä, Tero Kiuru, Olli Luukkonen and Prof. Constantin Simovski, just to name a few.

Also, to not forget what is really important, I would like to thank my friends, family and those fellow students that worked at the University at the warm summer of 2007, you gave me a lot to think and carry on!

Otaniemi, 19.5.2008

Antti Karilainen

Contents

Symbols and Abbreviations

Symbols

f	frequency
h	height
j	imaginary unit
k	wave number
$\mathbf{k}$	wave vector
l	length
n	integer
r	distance from the origin in spherical coordinates
$\mathbf{r}$	position vector of a field point
$\mathbf{r}'$	position vector of a source point
$\mathbf{u}$	direction unit vector
v_g	group velocity
v_p	phase velocity
w	width
x	x-axis in cartesian coordinates
y	y-axis in cartesian coordinates
z	z-axis in cartesian coordinates
AF	array factor
$\mathbf{B}$	magnetic flux density
C	capacitance
D	directivity of an antenna
$\mathbf{D}$	electric flux density
$\mathbf{E}$	electric field strength
F	radiation pattern
G	gain of an antenna
G_0	free-space Green function
$\overline{\overline{G}}$	Green dyadic
$\mathbf{H}$	magnetic field strength
I	complex current
$\overline{\overline{I}}$	unitary dyadic
$\mathbf{J}$	electric surface current
$\mathbf{J}_m$	magnetic surface current
$\mathbf{K}$	tangential wave vector at an interface of two materials
L	inductance
M	a point in the Brillouin diagram
$\mathbf{N}$	radiation vector

(Continued on the next page)

Symbols, Continued

P	power
$\overline{\overline{P}}$	projection dyadic
R	resistance
S_{mn}	mn'th element of a scattering matrix of an N-port
V	complex voltage
W	radiated power
X	reactance, or a point in the Brillouin diagram
Z	impedance ($Z = R + jX$)
Z_0	characteristic impedance of a waveguide
α	attenuation factor
β	phase propagation constant
δ	phase delay
ϵ	permittivity of a material ($\epsilon = \epsilon_r \epsilon_0$)
ϵ_0	permittivity of vacuum
ϵ_{eff}	effective permittivity in quasi-TEM transmission lines
ϵ_r	relative permittivity of a material
η	wave impedance in a medium
η_0	wave impedance of vacuum
η_r	radiation efficiency
γ	complex propagation constant
θ	elevation angle in spherical coordinates, or electric length of a TL
λ	wavelength
μ	permeability of a material ($\mu = \mu_r \mu_0$)
μ_0	permeability of vacuum
μ_r	relative permeability of a material
ϕ	azimuth angle in spherical coordinates
ω	angular frequency
ρ	distance from the origin in plane
Γ	a point in the Brillouin diagram
Ω	full angles θ and ϕ in spherical coordinates

Operators

∇f	gradient of a function f
$\nabla \cdot \mathbf{E}$	divergence of a vector $\mathbf{E}$
$\nabla \times \mathbf{E}$	curl of a vector $\mathbf{E}$
$\nabla\nabla G$	gradient and divergence of a function G
$\overline{\overline{G}} \cdot \mathbf{E}$	relates a source vector $\mathbf{E}$ to a field point across free space
$\overline{\overline{P}} \cdot \mathbf{E}$	extracts the perpendicular component of a vector $\mathbf{E}$
$\int_S$	surface integral
$\int_V$	volume integral

Abbreviations

1-D	one-dimensional
2-D	two-dimensional
3-D	three-dimensional
ABCD	transmission matrix
ADS	Advanced Design System 2005A circuit simulator [1]
BW	backward wave
CRLH	composite right/left-handed
DNG	double negative
E-plane	A plane on which the electric field oscillates
ENG	epsilon negative
FEM	finite element method
FW	forward wave
H-plane	A plane on which the magnetic field oscillates
HFSS	HFSS 10.1.3 full-wave electromagnetic simulator [2]
HIS	high-impedance surface
LH	left handed
LW	leaky wave
LWA	leaky-wave antenna
MATLAB	MATLAB 7.1.0.246 (R14) language for technical computing [3]
NRI	negative refractive index
SMD	surface-mount device
TEM	transverse electric and magnetic field
TKK	Helsinki University of Technology
TL	transmission line
TLN	transmission-line network
PEC	perfect electric conductor
QTEM	quasi-TEM

1 Introduction

Backward-wave (BW) materials, a special class of metamaterials with effective permittivity ϵ and permeability μ negative, have brought new and exciting promises in antenna applications, where antenna size could be made smaller or new kind of behaviour achieved with old structures. TKK's former Radio Laboratory and current Department of Radio Science and Engineering does research in new electromagnetic materials, including BW materials. BW materials are composed of normal conductors, dielectrics and magnetic materials, but they can be engineered to have unusual properties, different from materials found in nature. One of these exotic properties is the apparent reversal of Snell's law. Inside a normal material, phase velocity is usually in the same direction as the power flow (forward wave, FW), but with BW materials the phase velocity is directed in the opposite direction.

One efficient way to manufacture BW materials is to load a normal transmission line (TL) with extra inductance and capacitance, and then repeat this pattern. If the wavelength is several times larger than the loading elements and the period of the repeating pattern, the transmission-line network (TLN) appears as a homogeneous material with both FW and BW properties at different frequencies. Reversed phase velocity means reversed phase propagation constant, and, for example, in some antenna applications radiation can be directed to the opposite direction than with conventional solutions. From now on in the text we include loaded transmission lines in the concept of BW materials.

It turns out that between FW and BW regions power flow is still possible regardless of zero propagation constant. This makes planar antennas with broadside radiation possible. To manufacture a conformal antenna with high directivity, a complicated feeding system has been required before. Now, with near-zero phase propagation constant, the structure can be made simpler while preserving the directive properties.

A conformal antenna would in the simplest case work with just one simple waveguide feed, without any other feed network that takes space. When a wave is fed to the TLN system, it would radiate uniformly from every point with the same phase, thus producing a narrow beam of radiation. Also, the size of the conformal antenna would not affect its properties because of the zero phase propagation constant. At the beginning, a center feed would seem attractive, considering the size independence in the plane. Existing literature however discusses this option, and the results are not promising considering the broadside radiation in case of BW TLN materials. There are other options available to feed a conformal antenna, but what they gain in functionality, they lack in simplicity.

In this work we study conformal TLN antennas, and in particular study if a simple feed can be realized. Also, other interesting results about TLNs and knowledge about BW antennas are welcome.

2 Literature Review

Metamaterials became quickly a very popular research topic after J. B. Pendry discussed the possibility of achieving negative refraction in 2000. The phenomena was first brought up by Veselago in 1967, and after that, many "special materials" which can be covered by the word metamaterial were invented. Amongst the many applications where metamaterials, or backward-wave (BW) materials, are used, are antennas. By incorporating BW materials into existing antenna structures and types, for example size reduction and new directive properties are achieved. We will first take a look at the history of BW materials and then inspect the antenna applications invented so far.

2.1 History of Metamaterials

Material with simultaneously negative permittivity and permeability, named Veselago media, is usually the focus of current metamaterial discussion. Veselago predicted in 1967 that numerous new phenomena are linked to this unnatural property, that he named *left-handed* (LH), here are a few mentioned [4, 5, 6]:

- Reversed boundary conditions at the interface of normal and left-handed material
- Negative refraction at the the interface of normal and left-handed material
- Point source transformed into a point image by a slab of left-handed material

It took more than thirty years before Pendry showed in [7] that this kind of material with negative effective material parameters could make a perfect lens. Further study was provided by Smith & Kroll in [8], although with no material realization. This kind of material was based on a two-dimensional (2-D) array of repeated unit cells of copper strips and split-ring resonators, and it was first realized and measured by Shelby et al. in 2001 [9]. After that, there has been some discussion about the naming of such material [10], but our research group has settled for *backward-wave* (BW) medium [11]. This was argued to be better because a propagating plane wave in a BW material has "The Poynting vector and the wave vector pointing in the opposite lateral directions". Other names used are *negative refractive index material* (NRI), *double negative* (DNG) and *composite right/left-handed material* (CRLH, for BW TLN's), for example.

The non-resonant type of BW materials was introduced by Eleftheriades et al. and Caloz and Itoh, when they proposed to use loaded TLNs as a planar 2-D BW material [12, 13, 14]. A conceptual structure can be seen in Fig. 1, where a unit cell of length d is presented with a shunt admittance Y at the middle and a series impedance Z in series. This is the so called symmetrical structure, since Z has been distributed evenly at both sides of Y in both axial directions.

Three-dimensional (3-D) TLN-based BW materials were introduced a couple of years later [15, 16], with the necessary equations to solve the dispersion of such infinite TLNs. The structure can look basically the same as the 2-D counterpart, with TLs and series impedances also in the vertical direction.

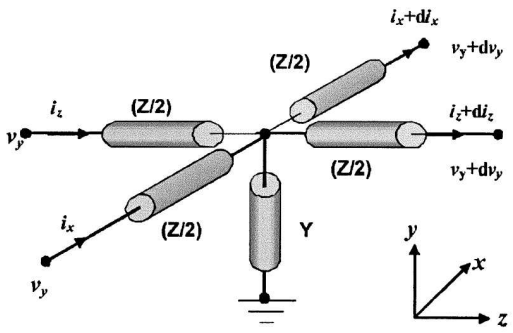

Figure 1: A unit cell for a 2-D distributed L-C network [12].

2.2 Overview of BW Material Antennas

The idea to use BW media in antenna applications was presented by Enoch et al. [17] and by Grbic et al. with measurements in 2002 [18, 19]. Enoch et al. used layers of copper grids to produce a slab of BW material, and then placed a dipole antenna inside it to have a narrow cone of radiation. Grbic et al. used a one-dimensional (1-D) loaded TLN network to have a BW frequency region, which made a backfire leaky-wave antenna (LWA) possible [18]. A unit cell of the antenna is presented in Fig. 2, which shows the microstrip realization of gap capacitors and stub inductors. Backfire LWA was soon developed into a continuous scanning backfire to end-fire LWA [20], see Fig. 3. The microstrip TL is not the only type of waveguide to construct an LWA: a rectangular waveguide antenna with one face corrugated has also been designed in [21].

The region between the FW and BW regions in the dispersion diagram of loaded TLNs has usually a band gap, i.e. no transmission is allowed at these frequencies. However, by matching the loaded TLN's loads L and C to the characteristic impedance of the TLs Z_0, a *balanced resonance* is achieved that permits the propagation and non-zero group velocity v_g at all frequencies in this region, even if the tangential wave number $\beta = 0$ [22]. This makes e.g. broadside radiation possible using the fundamental space harmonic, which is not realizable with normal leaky-wave antennas [6].

Allen et al. combined 1-D arrays of BW TLN into a semi-two-dimensional planar antenna with basically the same capabilities than the 1-D counterpart [23]. The structure was fed from one edge, while the other edges were terminated, as shown in Fig. 4. The downside of such planar antenna is the feed network. Wilkinson power dividers [24] were used to divide the power into four branches. This means

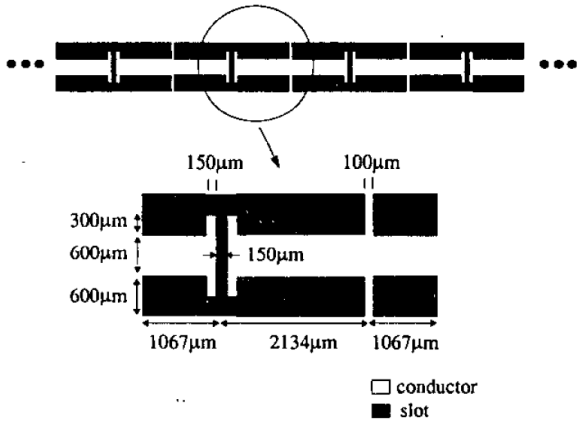

Figure 2: A 1-D TLN leaky-wave antenna is formed of transmission lines, gap capacitors and stub inductors [18].

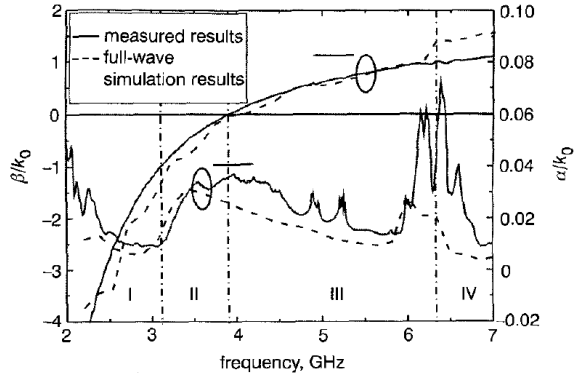

Figure 3: A frequency scanning one-dimensional LWA has backfire, broadside and end-fire radiation [20].

that a large area is sacrificed to the feed network. It was argued, however, that by controlling the feed amplitudes and phases, the beam could be made steerable also in the orthogonal direction. In this case a complex feeding network is unavoidable.

Another approach to planar antenna applications is the so called *mushroom* or *Sievenpiper structure*, which is a high-impedance surface (HIS) with a forbidden frequency band in the dispersion diagram [25], see Fig. 5. It has been used as an antenna ground plane and also described as a "first 2D leaky-wave antenna" [26]. However, a conical beam was produced, since the feed was placed at the center of the 2-D HIS. The waves spread radially from the feed with destructive interference in the normal direction in the far field. The mushroom structure does not seem to have a balanced condition between BW and FW regions in the dispersion diagram, so it is not as well suited for LWAs as TLNs. An equivalent transmission-line structure can be found for the mushroom structure though, so the difference with TLNs is not very big (Fig. 6(a)) [27].

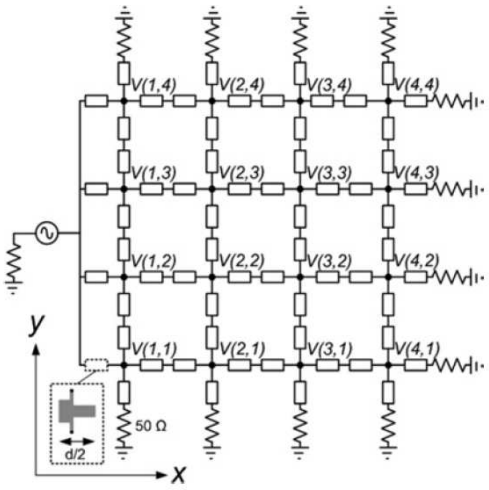

Figure 4: A LWA fed from one edge is made of a 2-D TLN [23].

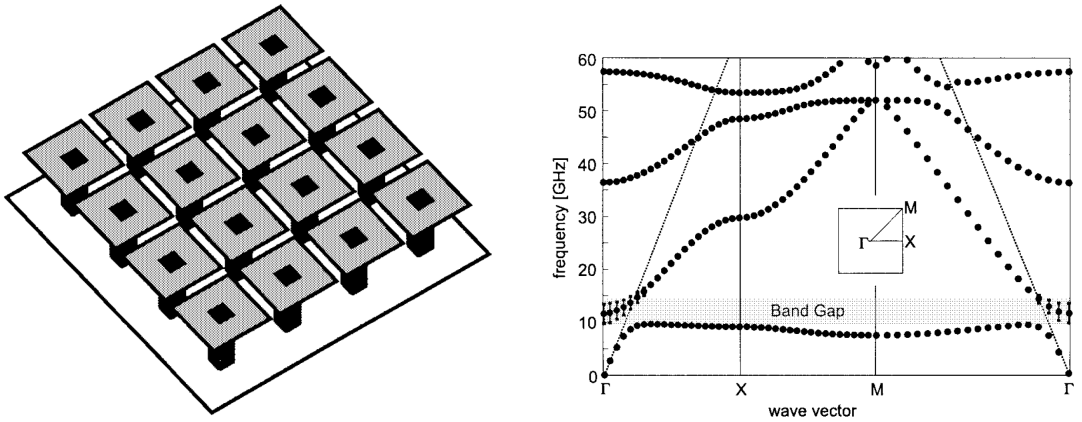

(a) (b)

Figure 5: a) Sievenpiper (mushroom) HIS [25]. b) Sievenpiper surface dispersion in the Brillouin zone [26].

Curiously, perhaps the first idea of an antenna using a slab of a BW material was briefly mentioned in 2001 [11, 28]. When discussing the Zenneck wave at the interface between two isotropic media, it was stated that if the other side of the interface was BW material, the real part of Poynting's vector tangential component points to the opposite directions on the two sides of the interface. After this, a slab or a cylinder of BW material acting as a wave guide would support backfire radiation.

BW antennas do not have to be based on leaky-wave propagation. Since $\beta = 0$ is possible, normal resonance-based antennas can be made smaller using the zeroth-order resonance mode [29], which is in theory length-independent. Also, zeroth-order resonance is confirmed to appear in both epsilon negative (ENG) and BW structures [30]. BW TLN structures are also used in feeding conventional antennas [31], but this is out of the scope of this thesis.

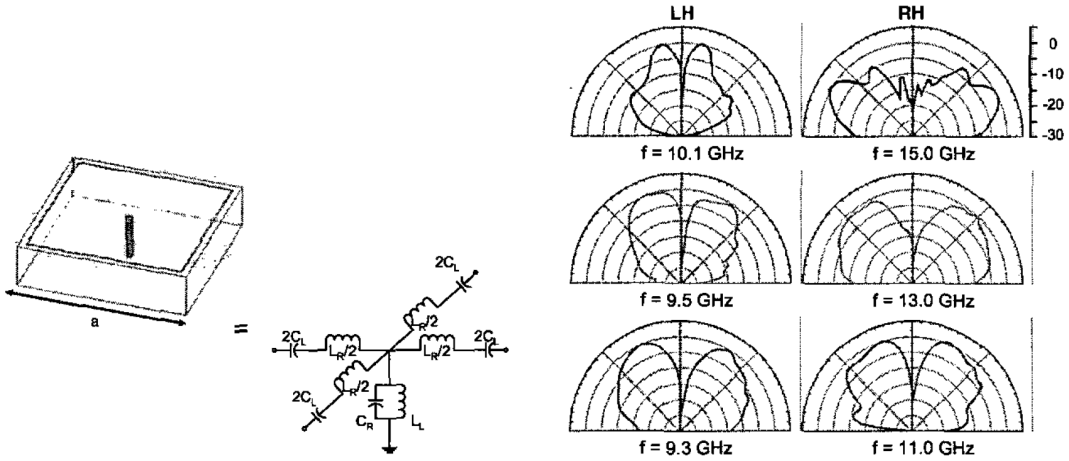

(a) (b)

Figure 6: A center-fed 2-D leaky-wave antenna. a) Mushroom type unit cell and equivalent circuit. b) Radiation patterns at different frequencies. [26]

If the scope of planar antennas is extended beyond antennas based on BW materials, many proposed structures can be found. For example, broadside radiation from periodic planar LWAs is treated analytically in rather recent papers [32, 33, 34]. These papers assume anti-symmetric excitation and an unbounded slab, and are not directly to the author's knowledge applicable to finite 2-D TLN antennas.

3 Theory

In this section we first review the basic Maxwell's equations and the surface wave solution at an air-surface interface, that is related to some antenna applications. Then we go through the essential antenna theory and properties. Since loaded transmission lines are the basis of this research, we also write the design equations for them. Finally, we study the dispersion in planar 1-D and 2-D TLN structures and see that BW and beta-zero propagation is possible within certain limits.

3.1 Maxwell's Equations and Plane Waves

Electromagnetic radiation is modelled with time-harmonic Maxwell's equations. Time dependent electric and magnetic fields are replaced by phasors with time dependency $e^{j\omega t}$, so differentiation with respect to time is transformed into a multiplication:

$$\nabla \times \mathbf{E} = -j\omega\mu\mathbf{H} - \mathbf{J}_m, \tag{1}$$
$$\nabla \times \mathbf{H} = j\omega\epsilon\mathbf{E} + \mathbf{J}. \tag{2}$$

Here $\mathbf{E}$ and $\mathbf{H}$ are electric and magnetic field strengths, respectively. Corresponding field sources are electric and magnetic current densities are denoted by $\mathbf{J}$ and $\mathbf{J}_m$ [35].

Helmholtz Equation

When we solve $\mathbf{H}$ from (1) and substitute it to (2), we get in a region with no sources

$$(\nabla^2 + k^2)\mathbf{E} = 0, \tag{3}$$

which is called the scalar *Helmholtz equation* for electric field. Here $k^2 = \omega^2\mu\epsilon$ [36].

Plane Waves

If we assume in (3) that the wave travels only in the z-direction, we can substitute the Helmholtz equation by an ordinary differential equation

$$\left(\frac{d^2}{dz^2} + k^2\right)\mathbf{E}(z) = 0, \tag{4}$$

whose solution is a linear combination of two exponential functions:

$$\mathbf{E}_+ e^{-jkz} + \mathbf{E}_- e^{jkz}. \tag{5}$$

These are called plane waves, traveling in positive and negative directions of the z-axis, respectively. Polarization of a plane wave is determined from the complex coefficients $\mathbf{E}_\pm$ [36].

Let us denote the plane-wave field as

$$\mathbf{E}(\mathbf{r}) = \mathbf{E}_0 e^{j\mathbf{k}\cdot\mathbf{r}}, \tag{6}$$

where $\mathbf{r}$ is the position vector and the wave vector $\mathbf{k} = k\mathbf{u}$, while $\mathbf{u}$ is the direction unit vector. Eq. (6) is similar for the magnetic field $\mathbf{H}(\mathbf{r})$. Substituting $\mathbf{E}(\mathbf{r})$ and $\mathbf{H}(\mathbf{r})$ into Maxwell's equations (1) and (2), we get

$$\mathbf{E}_0 = \frac{\mathbf{k}}{\omega\epsilon} \times \mathbf{H}_0, \tag{7}$$

$$\mathbf{H}_0 = -\frac{\mathbf{k}}{\omega\mu} \times \mathbf{E}_0. \tag{8}$$

Complex vector coefficients $\mathbf{E}_0$, $\mathbf{H}_0$ and $\mathbf{k}$ define the plane wave and they form an orthogonal vector triplet. Since $\mathbf{E}_0 \cdot \mathbf{k} = 0$ the magnetic field vector $\mathbf{H}_0$ is fully defined [37].

Plane wave behaviour can be classified into different cases. A plane wave is homogeneous if the direction vector $\mathbf{u} = \mathbf{k}/k$ is real, otherwise it is inhomogeneous. Additionally, the wave vector $k = \mathbf{k}/\mathbf{u}$ can be complex, if the wave number $k = \omega\sqrt{\mu\epsilon}$ is complex. All this relates to plane waves at an interface of e.g. two materials. Wave vector $\mathbf{k}$ can be depicted generally as an ellipse with the real and imaginary parts $\mathbf{k}_r$ and $\mathbf{k}_i$ lying on it and pointing at different directions. When a wave propagates along an interface, $\mathbf{k}_r$ tells the direction normal to the propagating phase fronts and $\mathbf{k}_i$ the direction where the field growth is strongest. The latter can be seen by studying Poynting's vector [37]

$$\mathbf{S} = \frac{1}{2}\mathbf{E} \times \mathbf{H}^* = \mathbf{S}_0 e^{2\mathbf{k}_i\cdot\mathbf{r}}. \tag{9}$$

This is important, since we immediately see the direction of radiation, if it is away from an interface.

3.2 Antenna Theory

Antennas cover a wide range of types of devices that transfer guided waves into radiating waves in free space, and their operation principles vary. Here we take a look first at the fundamental equations that tell how radiation is produced, and then we focus on concepts of antenna design, that are needed in this thesis.

Radiation of an Antenna

Field radiated by an antenna can be calculated from current densities $\mathbf{J}$ and $\mathbf{J}_m$. For simplicity, let us consider first only the electric current density $\mathbf{J}$. To take into account the field at position $\mathbf{r}$ from every source point $\mathbf{r}'$, we must integrate $\mathbf{J}$

over the whole source volume. The basic equation for radiation can be written to calculate the time-harmonic electric field at point $\mathbf{r}$ from an arbitrary current $\mathbf{J}$ [38]:

$$\mathbf{E}(\mathbf{r}) = -j\omega\mu \int_V \overline{\overline{G}}(\mathbf{r}-\mathbf{r}') \cdot \mathbf{J}(\mathbf{r}')dV', \tag{10}$$

where $\overline{\overline{G}}(\mathbf{r}-\mathbf{r}')$ is the Green dyadic, which maps the vector from point $\mathbf{r}'$ to point $\mathbf{r}$. In this case, it tells how we get the electric field $\mathbf{E}$ from current density $\mathbf{J}$. The Green dyadic can also be written as

$$\overline{\overline{G}}(\mathbf{r}-\mathbf{r}') = \left(\overline{\overline{I}} + \frac{1}{k^2}\nabla\nabla\right) G_0(\mathbf{r}-\mathbf{r}'), \tag{11}$$

where $k = \omega\sqrt{\epsilon\mu}$ is the wave number, $\overline{\overline{I}}$ is the unitary dyadic and $G_0(\mathbf{r}-\mathbf{r}')$ is the free-space Green function

$$G_0(\mathbf{r}-\mathbf{r}') = \frac{e^{-jk|\mathbf{r}-\mathbf{r}'|}}{4\pi|\mathbf{r}-\mathbf{r}'|}. \tag{12}$$

We can still make some approximations, and write the antenna's radiated field far from the source point as

$$\mathbf{E}(\mathbf{r}) = -j\omega\mu\frac{e^{-jkr}}{4\pi r}\overline{\overline{P}} \cdot \mathbf{N}(\mathbf{u}_r), \tag{13}$$

where $\mathbf{u}_r$ is the direction to the field point from the origin. $\mathbf{N}(\mathbf{u}_r)$ is the radiation vector, $\overline{\overline{P}}$ is the projection dyadic and r is the distance from the antenna. When operating with the dot product, the projection dyadic gives the perpendicular component of the radiation vector. The radiation vector can be written as

$$\mathbf{N}(\mathbf{u}_r) = \int_V e^{jk\mathbf{u}_r\cdot\mathbf{r}'}\mathbf{J}(\mathbf{r}')dV'. \tag{14}$$

Normally the magnetic field can be calculated from Faraday's law using (1), but an equation can also be derived:

$$\mathbf{H}(\mathbf{r}) = \int_V \nabla G(\mathbf{r}-\mathbf{r}') \times \mathbf{J}(\mathbf{r}')dV'. \tag{15}$$

Similarly as with the electric field, the magnetic field far from the source can be written:

$$\mathbf{H}(\mathbf{r}) = -jk\frac{e^{-jkr}}{4\pi r}\mathbf{u}_r \times \mathbf{N}(\mathbf{u}_r). \tag{16}$$

So, the radiation of an antenna is determined by the current density $\mathbf{J}$, from which we can determine the exact field with (10), or easier the far field with (13). If magnetic surface current $\mathbf{J}_m$ is used as a source, it is enough to replace the electric field $\mathbf{E}$ with magnetic field $\mathbf{H}$ in equations (10)-(16) because of duality.

Radiation Pattern and Polarization

The normalized radiation pattern of an antenna is defined with the normalized absolute value of the electric field in the far field:

$$F(\mathbf{u}_r) = \frac{|\mathbf{E}(\mathbf{r})|}{|\mathbf{E}(\mathbf{r})|_{\max}}. \tag{17}$$

The directivity can be calculated from the radiation pattern, and it is a function of direction, that tells how the antenna radiates power $W(\mathbf{u}_r)$ to different directions compared to an isotropic radiator. An isotropic radiator radiates power P_r evenly to every (solid angle) direction $\Omega = 4\pi$. The directivity can be calculated directly from the electric field, or by using Eq. (17):

$$D(\mathbf{u}_r) = \frac{W(\mathbf{u}_r)}{P_r/4\pi} = 4\pi\frac{|\mathbf{E}(\mathbf{r})|^2}{\int_S |\mathbf{E}(\mathbf{r})|^2 d\Omega} = 4\pi\frac{F^2(\mathbf{u}_r)}{\int_S F^2(\mathbf{u}_r) d\Omega}. \tag{18}$$

The gain of an antenna is the directivity multiplied by the radiation efficiency η_r of the antenna, which tells the ratio of the radiated power P_r and the power fed to the antenna P_{in}, and it is a function of direction just like the directivity:

$$G(\mathbf{u}_r) = \eta_r D(\mathbf{u}_r) \tag{19}$$

The difference between the gain and the directivity is that shile the total radiated power P_r was compared to radiated power as a function of direction $W(\mathbf{u}_r)$ in case of the directivity, in case of the gain the power fed to the antenna P_{in} is compared to the radiated power $W(\mathbf{u}_r)$.

Eqs. (18) and (19) give the directivity and the gain to all directions, but usually the maximum value in the direction of the main beam is only given. The radiation pattern $F(\mathbf{u}_r)$, the directivity D and the radiation efficiency η_r are of course functions of the frequency as well.

Electric and magnetic fields radiated by an antenna even in the far field have non-zero radial components, but locally these waves can be considered as plane waves. Polarization tells how the electric field vector rotates when the wave propagates in the far field. Polarization can be determined from the complex phasors, or from the real time-varying electric fields. Time-varying field can always be calculated from the real part of the product of the phasor and the time dependency $e^{j\omega t}$.

If the electric field vector draws an elliptic curve when propagating, the polarization is elliptic. If the axial ratio is 1:1, the field is circularly polarized. And finally, if either one of the axes of the ellipse is zero, the polarization is linear. In radio engineering the handedness of the wave tells if the electric field vector turns as the right or left hand's fingers when the thumb is pointing in the direction of propagation [38].

Aperture Antenna

Antennas, which have some kind of apertures through which the input power is radiated to space, are called aperture antennas. The radiation can be determined with the help of *Huygens' principle* (or, the *equivalence principle*) [35, 38]. The electric and magnetic field of the antenna can be covered by a surface S with equivalent electric and magnetic currents

$$\mathbf{J} = \mathbf{n} \times \mathbf{H}, \tag{20}$$

$$\mathbf{J}_m = -\mathbf{n} \times \mathbf{E}, \tag{21}$$

so that the field outside surface S is the same. If the electric and magnetic fields exist only at the aperture, equations (13) or (16) can be used to calculate the radiation in the far zone. Since the equations resemble Fourier integrals, there is a link between the aperture distribution of the fields and the radiation pattern in the far zone through the Fourier transformation [38]. For example, open end of a rectangular waveguide has some field distribution, and since it is a planar surface, the Fourier transformation can be solved analytically by separating the orthogonal components.

Antenna Array

Some times a narrow main beam is desired from an antenna. This cannot be realized with a small antenna relative to radiated wavelength, but the main beam can be made narrower by combining several antennas into an antenna array. A group of similar antennas or antenna elements is called an antenna array if the currents in the elements satisfy

$$\mathbf{J}_n(\mathbf{r}) = a_n \mathbf{J}_0(\mathbf{r} - \mathbf{r}_n). \tag{22}$$

Current of an element n can be determined by moving the initial element's current $\mathbf{J}_0$ by a vector $\mathbf{r}_n$ and multiplying it with a complex number a_n [38]. That is, changing the amplitude and the phase of the current. This means that the antenna elements cannot be rotated relative to one another and all the elements must point in the same direction.

If the far zone of more than one element is considered, we see that in (13) it is enough to study only the radiation vector

$$\mathbf{N}_n(\mathbf{u}_r) = \int_{V_n} e^{jk\mathbf{u}_r \cdot \mathbf{r}} \mathbf{J}_n(\mathbf{r}) dV, \tag{23}$$

where V_n is the volume occupied by the n'th element. Radiating vector of each element is then given by moving the initial element $\mathbf{N}_0$ to a point $\mathbf{r}_n$ and multiplying it with a_n:

$$\begin{aligned} \mathbf{N}_n(\mathbf{u}_r) &= a_n \int_{V_n} e^{jk\mathbf{u}_r \cdot \mathbf{r}} \mathbf{J}_0(\mathbf{r} - \mathbf{r}_n) dV \\ &= a_n \int_{V_0} e^{jk\mathbf{u}_r \cdot (\mathbf{r}' + \mathbf{r}_n)} \mathbf{J}_0(\mathbf{r}') dV' \\ &= a_n e^{jk\mathbf{u}_r \cdot \mathbf{r}_n} \mathbf{N}_0(\mathbf{u}_r). \end{aligned} \tag{24}$$

Here V' refers to integration over the source points of the initial element. Following the same procedure, the far field is

$$\mathbf{E}_n(\mathbf{r}) = a_n e^{jk\mathbf{u}_r\cdot\mathbf{r}_n}\mathbf{E}_0(\mathbf{u}_r), \tag{25}$$

where $\mathbf{E}_0$ is the far field of the initial element. In (25) we see directly the change in the amplitude and phase produced by moving of an element. If the antenna array has N elements, the far field of the whole array is given by

$$\mathbf{E}(\mathbf{r}) = \sum_{n=1}^{N} a_n e^{jk\mathbf{u}_r\cdot\mathbf{r}_n}\mathbf{E}_0(\mathbf{r}) = AF(\mathbf{u}_r)\mathbf{E}_0(\mathbf{r}), \tag{26}$$

where function $AF(\mathbf{u}_r)$ is called the element-independent array factor. Even if separate antennas are not used, antenna array concept can be utilized to study the properties of otherwise complex structures.

Leaky-Wave Antennas

Leaky-wave antennas (LWAs) are a subclass of travelling-wave antennas. If a wave travels in a, say, planar structure, then the tangential component $\mathbf{K}$ of the wave vector $\mathbf{k}$ is continuous across the interface. This is illustrated in Fig. 7. The plane-wave solution above the interface then has the same tangential component, and as well an orthogonal component k_z [37, 38]. The wave vector above the interface is then of the form

$$\mathbf{k} = \mathbf{u}_x\beta + \mathbf{u}_z k_z, \tag{27}$$

where $\beta = k_x$. Then under the condition $\beta < k$ the normal component

$$k_z = \sqrt{k^2 - \beta^2} \tag{28}$$

becomes real (so called fast wave), and above the structure a plane wave propagates at the angle

$$\theta = \arcsin\frac{\beta}{k} \tag{29}$$

from the surface. This angle θ tells the direction of power propagation, which is away from the surface. If $\beta > k$, the normal component is imaginary and the wave decays exponentially normal to the interface. This kind of wave is called slow wave, which does not radiate unless there are some discontinuities or the waveguide ends.

In the fast-wave case, due to the radiated power, the propagation constant becomes complex and the wave amplitude decays exponentially with the so called attenuation factor α. We can consider the field at each point x of the structure as aperture distribution $|\mathbf{E}| \sim e^{-\alpha x}$. If the radiating structure is uniform, the power decays exponentially. If α is large, most of the power is radiated before the end of the structure, and the whole aperture is not utilized. On the other hand, if α is small, a large part of the power does not have the time to radiate before the wave reaches the end of the structure. By shaping the structure so that $\alpha = \alpha(x)$ varies at the

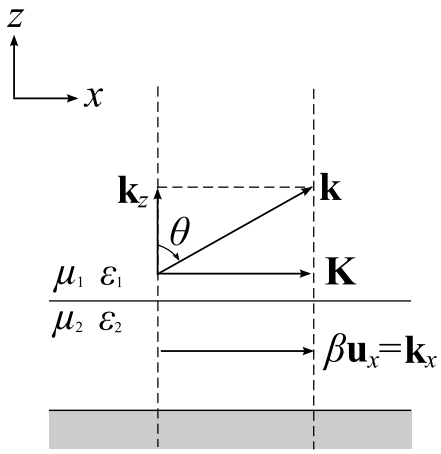

Figure 7: Interface with continuous tangential component $\mathbf{K}$ of the wave vectors below and above the interface.

wanted aperture, the aperture distribution $|\mathbf{E}|$ can be shaped to produce lower side lobes for the radiation beam [38].

If losses are included in the structure, Eqs. (27) and (28) are more complicated. Normally, if the attenuation factor α is small, we would replace $\beta \to \beta - j\alpha$ and use the Taylor/Maclaurin series expansion [39]

$$\mathbf{k} \approx \mathbf{u}_x\sqrt{\beta - j\alpha} + \mathbf{u}_z\left(\sqrt{k^2 - \beta^2} + j\frac{\alpha\beta}{\sqrt{k^2 - \beta^2}}\right), \tag{30}$$

to see that since the $\mathbf{u}_z$ component has a positive imaginary part, field actually grows away from the structure up to some distance due to Eq. (9). This seemingly unphysical result is seen only locally due to the infinite approximation [38]. The real part is still positive, so the leaky-wave radiation is not disturbed. But what happens if β is the smallest term? Using the same series expansion (see Appendix A), we get

$$\mathbf{k} \approx \mathbf{u}_x(\beta - j\alpha) + \mathbf{u}_z\left(\sqrt{k^2 + \alpha^2} + j\frac{\alpha\beta}{\sqrt{k^2 + \alpha^2}}\right). \tag{31}$$

So, basically the situation is still the same, and leaky-wave radiation is possible. We see that exactly at $\beta = 0$ we have the real and imaginary wave vectors $\mathbf{k}_r$ and $\mathbf{k}_i$ lying at the axes of the ellipse used sometimes to illustrate a complex vector. Usually this is not the case with inhomogeneous wave vectors in lossy media [37].

Leaky-wave antennas themselves are divided into two subclasses: uniform and periodic. Uniform LWAs have a uniform structure along their length, whereas periodic LWAs have some periodic modulation [40]. Uniform LWAs naturally have some kind of a way for the fast wave to leave the structure, e.g. slit in a rectangular waveguide. Periodic LWAs have on the other hand a slow wave travelling in the structure. Because of the periodic perturbations, an infinite number of spatial harmonics is excited, some of them fast waves. Usually one of them is chosen to be the radiating harmonic. Earlier, periodic LWAs have been designed to work with the $n = -1$ spatial harmonic, but now with loaded TLNs $n = 0$ can be used.

3.3 Transmission-Line Theory

Transmission-line based BW antennas have both distributed transmission-line elements and lumped or distributed circuit elements. Here we review the basic properties and design equations for a normal TL, and the connection between the characteristic impedance and circuit parameters.

TEM and Quasi-TEM Transmission Lines

Transmission lines with two or more separate ideal conductors and homogeneous lossless filling materials are called TEM (transverse electric and magnetic field) waveguides. Waves in such structures travel at the same phase velocity

$$v_p = \frac{c}{\sqrt{\epsilon_r}} \tag{32}$$

similar to plane waves in the filling material, and therefore TEM transmission lines are dispersion free. If the conductor is not perfect electric conductor (PEC), or the filling is composed of two materials with different material parameters ϵ_r and μ_r, the waves travel at different velocities in the materials. This means that the structure is dispersive. However, usually the resulting wave mode differs only a little from the TEM mode. If the wave mode resembles the TEM mode when $\omega \to 0$, we call it a quasi-TEM (QTEM) wave mode. Microstrip TLs are widely used QTEM waveguides, with dielectric as a filling material and air above the strip.

An effective permittivity ϵ_{eff} can be defined for QTEM structures. If the air and the dielectric with ϵ_r of a microstrip structure is replaced by a homogeneous material with ϵ_{eff}, the velocity of the wave in the structure is the same as for a TEM mode in such structure. An approximate equation for the effective permittivity for a microstrip TL is

$$\epsilon_{\text{eff}} = \frac{\epsilon_r - 1}{2} + \frac{\epsilon_r + 1}{2} + \frac{1}{\sqrt{1 + 12h/w}}, \tag{33}$$

where h is the height of the substrate and w is the width of the microstrip [24]. The width or height of the microstrip can be calculated from

$$\frac{w}{h} = \begin{cases} \frac{8e^A}{e^{2A}-2} & w/h < 2 \\ \frac{2}{\pi}\left[B - 1 - \ln(2B-1) + \frac{\epsilon_r - 1}{2\epsilon_r}\left\{\ln(B-1) + 0.39 - \frac{0.11}{\epsilon_r}\right\}\right] & w/h > 2 \end{cases} \tag{34}$$

where

$$A = \frac{Z_0}{60}\sqrt{\frac{\epsilon_r + 1}{2}} + \frac{\epsilon_r - 1}{\epsilon_r + 1}\left(0.230 + \frac{0.11}{\epsilon_r}\right),$$
$$B = \frac{\eta_0 \pi}{2Z_0\sqrt{\epsilon_r}}.$$

Circuit Model of Transmission Lines

A transmission line is usually described with some electric length $\theta = \beta l$ and a characteristic impedance Z_0. A lumped element circuit model can present the same TL if it is a TEM or a QTEM transmission line. For a lossy TL (Fig. 8) the circuit model contains series inductance L' and resistance R' and shunt capacitance C' and conductance G'. R' corresponds to conductor losses and G' for substrate losses. These values are for a differential increment Δz of a TL, and if the values for a finite-sized TL are wanted, the parameters must be multiplied by the physical length l of the transmission line.

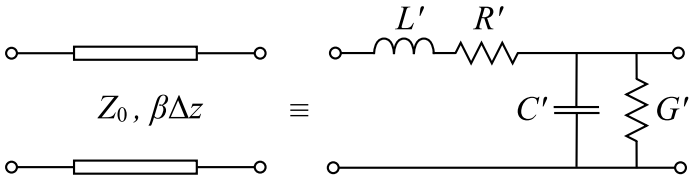

Figure 8: Equivalent circuit for a transmission line.

The propagation constant γ can be expressed also with the differential circuit parameters

$$\gamma = \alpha + j\beta = \sqrt{(R' + j\omega L')(G' + j\omega C')}, \tag{35}$$

and the characteristic impedance Z_0 similarly with

$$Z_0 = \sqrt{\frac{R' + j\omega L'}{G' + j\omega C'}}. \tag{36}$$

The wavelength in a transmission line, whether lossless or lossy, is defined as

$$\lambda = \frac{2\pi}{\beta}. \tag{37}$$

In a lossy case $\alpha > 0$, and the wave attenuates in the TL, for example in the z-direction, with exponential decay $e^{-\alpha z}$. If the TL is lossless $R' = G' = 0$, the propagation constant $\gamma = \alpha + j\beta$ reduces to $\gamma = j\beta$ so the wave amplitude is not attenuated [24].

In lossless TEM or QTEM transmission lines there is a connection between the characteristic impedance and the circuit parameters:

$$Z_0 = \frac{V}{I} = \sqrt{\frac{L}{C}} = \frac{L}{\mu}\eta = \frac{\epsilon}{C}\eta, \tag{38}$$

where permittivity $\epsilon = \epsilon_r\epsilon_0$ and permeability $\mu = \mu_r\mu_0$ depend on the filling material, and $\eta = \sqrt{\mu/\epsilon}$ is the wave impedance in the filling material [37].

Periodic Transmission Lines

If an eigenmode propagates in a periodic waveguide to the z-direction, the *Floquet theorem* tells that the field varies only by a complex coefficient when translated from z to $z + nd$:

$$\mathbf{E}(x, y, z + nd) = \mathbf{E}(x, y, z)e^{\gamma nd}, \tag{39}$$

where n is an integer, d is the period and γ is a complex constant [37, 5]. If we describe a unit cell of such a periodic structure with the ABCD parameters [24], we can write a periodic relation for voltages and currents at the n'th port:

$$\begin{bmatrix} V_n \\ I_n \end{bmatrix} = \begin{bmatrix} A & B \\ C & D \end{bmatrix} \begin{bmatrix} V_{n+1} \\ I_{n+1} \end{bmatrix} = \begin{bmatrix} V_{n+1}e^{\gamma d} \\ I_{n+1}e^{\gamma d} \end{bmatrix}, \tag{40}$$

where relations $V_{n+1} = V_n e^{-\gamma d}$ and $I_{n+1} = I_n e^{-\gamma d}$ were used. Solving the characteristic equation for the matrix in (40) leads to an equation for the propagation constant γ:

$$AD + e^{2\gamma d} - (A + D)e^{\gamma d} - BC = 0, \tag{41}$$

which reduces to

$$\cosh(\gamma d) = A, \tag{42}$$

if the circuit is symmetric ($A = D$) and reciprocal ($AD - BC = 1$). We can also solve the so called Bloch impedance

$$Z_B = \frac{V_{n+1}}{I_{n+1}}, \tag{43}$$

which tells us the relation between the voltage V and the current I of a mode in the infinite structure. However, this relation is defined only at certain points, at every unit cell length d from each other. Eq. (43) reduces again due to symmetry and reciprocity to

$$Z_B^{\pm} = \frac{\pm B}{\sqrt{A^2 - 1}}. \tag{44}$$

The correct sign for Z_B must be chosen for waves travelling in positive or negative direction along z.

Coaxial Waveguide

The power can be guided to an antenna with numerous waveguides, one popular being the coaxial cable, where usually a circular core is surrounded by a circular coating conductor. The characteristic impedance can be calculated with [35]

$$Z_0 = \frac{\eta_0}{2\pi\sqrt{\epsilon_r}} \ln\left(\frac{b}{a}\right), \tag{45}$$

where η_0 is the wave impedance of vacuum, ϵ_r is the relative permittivity of the filling material, b is the diameter of the coating conductor and a is the diameter of the core conductor.

Impedance and Scattering Parameters

An antenna can be thought as a one-port circuit element with its own input impedance [38]. This impedance is called the antenna impedance Z_a and it can be separated to the resistive and reactive parts. The resistive part is then divided into the loss resistance R_a and radiation resistance R_r, which portrays the power transmitted to radiated power. The reactive part describes the reactive fields around the antenna, which do not radiate.

Structures with ports are described also with scattering parameters S. The antenna impedance Z_a or the input impedance of the corresponding one port can be expressed as follows [41]:

$$S_{11} = \frac{Z_a - Z_0}{Z_a + Z_0} \quad \Leftrightarrow \quad Z_a = Z_0 \frac{1 + S_{11}}{1 - S_{11}}, \tag{46}$$

where Z_0 is the characteristic impedance of the waveguide feeding the antenna.

3.4 Theory of Transmission-Line Based Metamaterials

Loaded transmission lines can be considered as BW materials when the repeating unit cell structure is dense enough compared to the wavelength. The BW region is constructed by loading the TL with some extra capacitance C and inductance L. To achieve the opposite phase velocity direction in contrast to the direction of power propagation, the load elements must turn the phase of the travelling wave to the reverse direction compared to an ordinary TL. A unit cell of a symmetrical 1-D structure is presented in Fig. 9. The length of the unit cell is d, and C and L are the load capacitance and inductance values. 1-D TLN BW material is composed of adjacent unit cells. The structure can also be easily extended to a planar 2-D structure and even to a volumetric 3-D structure.

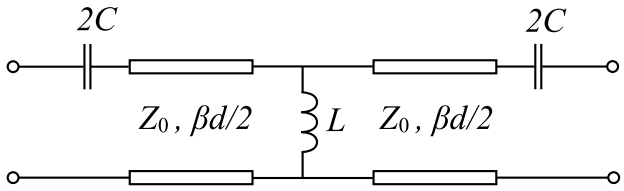

Figure 9: A symmetrical circuit presentation for a BW transmission-line unit cell.

Unbalanced and Balanced Dispersion

By applying the Floquet theorem, we can solve the dispersion for a 1-D TLN with the well-known Eq. (42), and draw a dispersion diagram of such a loaded TL structure with some values of L and C, which can be seen in Fig. 10(a). $\beta = \beta(k)$ is the propagation constant in the structure and $k = \omega\sqrt{\epsilon_0\mu_0}$. The straight line $|\beta| = k$ is the so called light line. Between the light lines the dispersion gives values $\beta < k$, and

this region is also the leaky-wave (LW) region, as seen from Eq. (28). The pass band of the structure is seen when β has some non-zero values, and the stop band when β is zero or imaginary (only real part is shown in the figure). The phase velocity is

$$v_p = \frac{\omega}{\beta} = c\frac{k}{\beta}, \tag{47}$$

from which we can see that when $\beta < k$, the phase velocity is faster than the speed of light c, and the structure supports leaky waves, i.e. fast waves. This region can be seen from Fig. 10(a) between the points where the dispersion curve intersects the light line. On the other hand, we can see the phase velocity v_p directly at any point just by calculating the slope of the straight line from the origin to a point at the curve and multiplying it with c.

Fig. 10(a) can be divided into three regions: Region where $\beta > 0$ and $v_p > 0$ is the forward-wave (FW) region, region with $\beta < 0$ and $v_p < 0$ is the backward-wave (BW) region, and between those we have a stop band, or a band gap, with $\beta = 0$. Stop band regions can also be found above the FW and below the BW regions. We call this case with a band gap between the BW and the FW regions as the *unbalanced* dispersion. Frequencies where these regions meet, are called cut-off frequencies. The FW region has a positive and the BW region has a negative phase velocity.

The group velocity is

$$v_g = \frac{d\omega}{d\beta} = c\frac{dk}{d\beta}, \tag{48}$$

which is the slope of the dispersion curve at any frequency f, or wave number k in our figure. From Fig. 10(a) we see that when the wave number approaches the stop band or cut-off, the group velocity approaches zero and no power propagates. When $\beta < 0$ the group velocity follows the slope at the negative side and is still positive contrary to the phase velocity, hence backward-wave propagation.

By introducing extra components L and C to the lossless TL equivalent circuit model of Fig. 8, we can draw Fig. 11. From the circuit topology we can see two LC resonators: the series resonator with the resonant frequency ω_{01} and the parallel resonator with ω_{02}. The resonance frequencies can be solved from equations

$$\omega_{01} = \frac{1}{\sqrt{L_{\mathrm{TL}}C}}, \tag{49}$$

$$\omega_{02} = \frac{1}{\sqrt{C_{\mathrm{TL}}L}}, \tag{50}$$

where L_{TL} is the inductance per unit length L' multiplied by the unit cell length d $L_{\mathrm{TL}} = L'd$, and C_{TL} the corresponding capacitance $C_{\mathrm{TL}} = C'd$. The characteristic impedance of the TL in lossy case would be

$$Z_0 = \sqrt{\frac{R' + j\omega L_{\mathrm{TL}} + \frac{1}{j\omega C}}{G' + j\omega C_{\mathrm{TL}} + \frac{1}{j\omega L}}}. \tag{51}$$

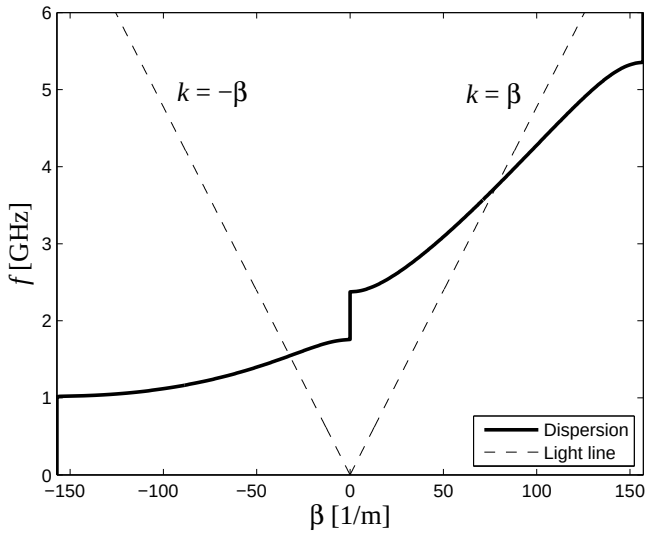

(a)

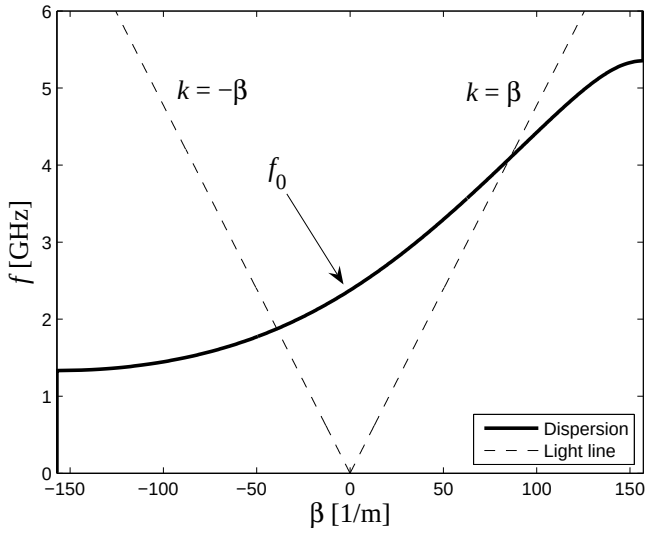

(b)

Figure 10: a) Unbalanced and b) balanced dispersion in the dispersion (k-β) diagram. The balanced dispersion with $f_0 = 2.38$ GHz is calculated with reactive load values $L = 2.00$ nH and $C = 0.80$ pF for a 1-D TLN, and with $Z_0 = 50\ \Omega$, $\epsilon_r = 1.96$ and $d = 20$ mm. For the unbalanced dispersion capacitance is doubled to $C = 1.60$ pF.

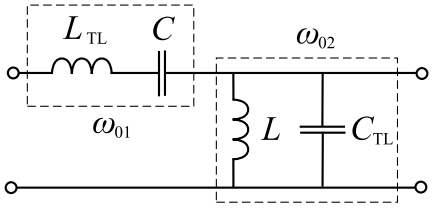

Figure 11: Equivalent circuit for a lossless BW transmission line.

Fig. 11 of course can be seen to have more LC resonance circuits, and we see in the next section that when cascaded, the unit cells produces multiple resonances.

If we choose the values of the loading components so that the resonant frequencies (49) and (50) are the same, interesting things happen. From Fig. 10(b) we see that the curve becomes continuous over $\beta = 0$ point at a certain frequency f_0. This means that the stop band disappears regardless of how small β is. The phase velocity v_p goes still to infinity and the wavelength λ also goes to infinity because of (37). The group velocity v_g follows the curve to the negative side through $\beta = 0$ and is not zero at any point. This means that the power propagates regardless of the zero phase velocity v_p [24].

This *balanced* dispersion is achieved in the 1-D case when

$$\sqrt{\frac{Z}{Y}} = Z_0 = \sqrt{\frac{L_{\mathrm{TL}}}{C_{\mathrm{TL}}}}, \tag{52}$$

where Z is the series impedance divided to the both sides of the symmetrical unit cell, and Y is the parallel admittance in the center of the unit cell. In ideal case these would represent C and L, correspondingly, but Z and Y can also include losses:

$$Z = \frac{1}{j\omega C} + R, \tag{53}$$

$$Y = \frac{1}{j\omega L} + G, \tag{54}$$

where R is resistance and G conductance (not to be mixed with the losses R' and G' of a TL). If the structure in Fig. 9 is two-dimensional, i.e. cross-shaped and connected at the inductor L, we have a superposition of two circuits. Because of the parallel connection of the two inductances we have the relation

$$\sqrt{\frac{Z}{2Y}} = Z_0, \tag{55}$$

when we want the balanced condition with the same f_0. The 3-D balanced condition follows directly using the same reasoning:

$$\sqrt{\frac{Z}{3Y}} = Z_0. \tag{56}$$

The design of the balanced case is then as follows. Fix the characteristic impedance Z_0 of the TL and either one of L or C. Then solve the missing load value from (52), (55) or (56) depending on the dimension of the wanted unit cell.

Dispersion for two or three dimensions is also solved in the literature, one example can be found in [16, 42]. The dispersion equation for the 3-D structure reads

$$\cos(k_x d) + \cos(k_y d) + \cos(k_z d) = \frac{Y}{2S} - 3\frac{K}{S}, \tag{57}$$

where

$$S = \frac{Z}{(ZA+B)(ZD+B) - B^2}, \tag{58}$$

$$K = \frac{Z(AD-BC)(ZA+B)}{(ZA+B)(ZD+B) - B^2} - \frac{A}{B}, \tag{59}$$

A, B, C and D are the transmission parameters for a lossless transmission line:

$$\begin{bmatrix} A & B \\ C & D \end{bmatrix} = \begin{bmatrix} \cos(\beta_{\mathrm{TL}} d/2) & jZ_0 \sin(\beta_{\mathrm{TL}} d/2) \\ jY_0 \sin(\beta_{\mathrm{TL}} d/2) & \cos(\beta_{\mathrm{TL}} d/2) \end{bmatrix}, \tag{60}$$

Z and Y are the load series impedance and shunt admittance, respectively, $\beta_{\mathrm{TL}} = \omega\sqrt{\epsilon_r}/c$ and $Y_0 = 1/Z_0$. Note, that the wavenumber in the z-direction is now a different wave number than the one in Eq. (27).

1-D and 2-D cases are obtained when we use only the desired wave vectors k_x, k_y or k_z and set the integer corresponding to the dimension in the last term of Eq. (57). To study the dispersion in two dimensions, we draw the *Brillouin diagram*, which is used in solid state physics to model periodic structures. Using equation (57), we can draw Fig. 12. $\Gamma \rightarrow X$ is the axial direction along the TLN with no phase shift, $X \rightarrow M$ is the 180-degrees phase shift and $M \rightarrow \Gamma$ is the diagonal direction with no phase shift. The Brillouin diagram defines the behaviour of the wave vector in the structure. More thorough explanation for the diagram can be found in [13].

A new type of Brillouin diagram for 1-D structures was suggested in [43], where leakage into surface waves and leaky waves are separated. This concerns mainly 1-D structures, where surface modes have a free path to travel away from the structure at the substrate-air interface.

We see that f_0 does not change whether moving along the axial or diagonal direction along the structure, as expected. However, if we move from Γ to X or M, we see the difference in the slope, i.e. the structure is not (in the $x-y$ plane, for example) isotropic at all frequencies.

The characteristic impedance or Bloch impedance Z_B of the infinite BW TLN also depends on the balanced condition. Characteristic impedance for 2-D and 3-D structures can be solved from equations in [16]. In Fig. 13(a) we have unbalanced dispersion with twice the capacitance C of the balanced dispersion, and Z_B shows a strong discontinuity at f_0. With the balanced condition, the discontinuity disappears and we get a smooth impedance behaviour near f_0, as seen in Fig. 13(b).

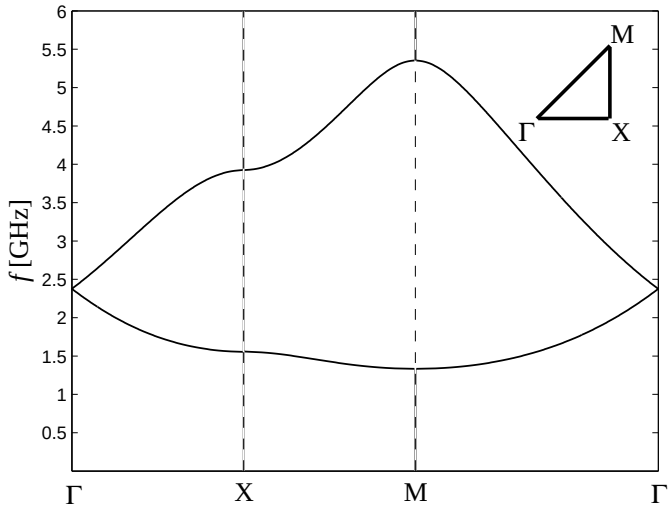

Figure 12: The Brillouin diagram for a balanced 2-D TLN ($f_0 = 2.38$ GHz), with reactive loads $L = 1.00$ nH and $C = 0.80$ pF, $Z_0 = 50\ \Omega$, $\epsilon_r = 1.96$ and $d = 20$ mm.

When designing TLN-based metamaterials, we need to have the unit cell size d small compared to the wavelength λ in the transmission-line structure. Even though the wavelength seems to go to infinity around f_0 in the balanced case, we have to remember that the wave still propagates along normal waveguides. The limit for a good approximation of homogeneity is suggested in [6] to be $d = \lambda/4$. Recent literature has however pointed out, that this homogeneity approximation does not always give the optimal results concerning the Bloch impedance for a finite structure [44].

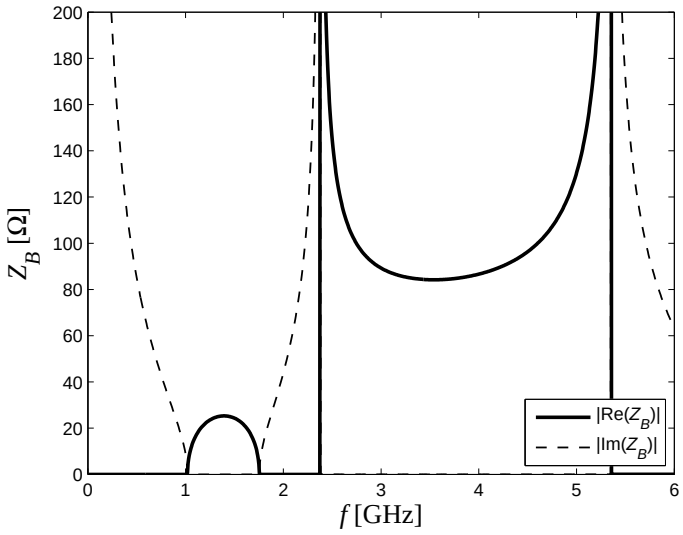

(a)

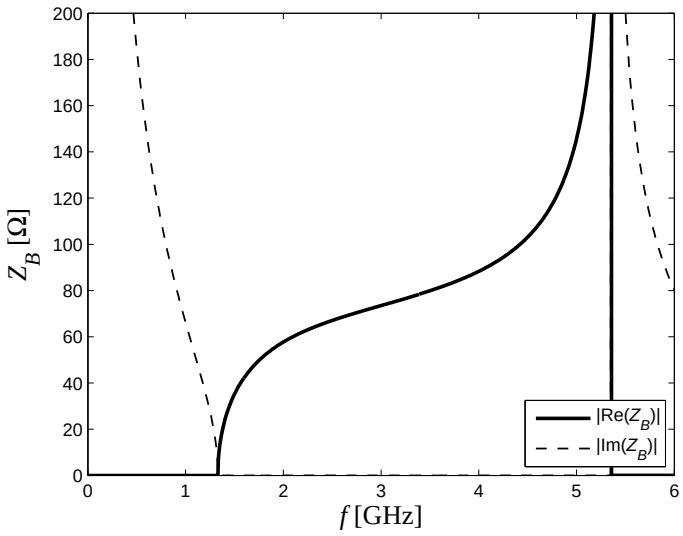

(b)

Figure 13: a) The Bloch impedance with unbalanced and b) balanced dispersion for a 1-D TLN. The balanced Z_B ($f_0 = 2.38$ GHz) is calculated with reactive load values $L = 2.00$ nH and $C = 0.80$ pF, and with $Z_0 = 50\ \Omega$, $\epsilon_r = 1.96$ and $d = 20$ mm. For the unbalanced Z_B capacitance is doubled to $C = 1.60$ pF.

4 Design of a 1-D TLN Antenna

In this section we design a 1-D BW TLN antenna following the theory of Section 3. We study the basic properties of such an antenna as well as the design guidelines. First we use an analytical dispersion model to calculate the matched parameter values for the 1-D case, and then we try to construct an analytical model of a finite TLN antenna. A finite-sized TLN antenna is simulated with a full-wave software to verify the operation.

4.1 Unit Cell Design

In order to design a proper unit cell operating at some f_0, we need to choose the used transmission-line structure. The microstrip TL is the logical choice since it is easy to manufacture and model. One of the commercially available substrates Rogers RT/Duroid 5870 used in the laboratory has the relative permittivity $\epsilon_r = 2.33$ and thickness $h = 0.787$ mm. We also have to fix the characteristic impedance Z_0 to calculate the width of the transmission line w from Eq. (34). Again, $Z_0 = 50\ \Omega$ is a widely used value for the impedance, and leads to $\epsilon_{\text{eff}} = 1.96$.

The length of the unit cell d as well as the loading parameters L and C have all an effect on f_0, but because L and C are connected through Z_0 in the balanced condition with Eq. (52), we have to only choose either one of those. A unit cell length $d = 20$ mm is large enough to still have space for inductances and capacitances, if they are lumped elements. Values for L and C for the balanced dispersion are presented in Table 1 with the corrsponding f_0. Also, bandwidth Δf and the Bloch impedance Z_B at f_0 are presented in each case. It should be noted that only with the values of the first row the wavelength in the substrate goes under the homogeneity limit discussed in the previous section. But since the TLN antenna does not rely on the concept of homogenizeable metamaterials, we can accept this unit-cell length.

We can see from Table 1 that the passband's upper frequency does not depend on L and C for the 1-D case. The Bloch impedance Z_B gets a little larger values than Z_0 at f_0 in this frequency region. Although we show here the results for $d = 20$ mm, this seems to hold for other values of d as well. There seems to be no way to achieve

Table 1: Values of L, C, f_0, pass band start f_1 and stop f_2, bandwidth Δf and Z_B at f_0 in balanced 1-D dispersion with $d = 20$ mm.

L [nH]	C [pF]	f_0 [GHz]	f_1 [GHz]	f_2 [GHz]	Δf [GHz]	Z_B [Ω]
1.0	0.40	3.10	2.07	5.36	3.29	81.4
2.0	0.80	2.38	1.33	5.36	4.03	65.3
2.2	0.88	2.28	1.24	5.36	4.12	63.7
3.3	1.20	1.97	0.92	5.36	4.44	59.7
3.6	1.44	1.84	0.80	5.36	4.56	58.3

$Z_0 = Z_B$ at f_0. If we let L grow while maintaining the balanced dispersion, β and Z_B close to those of an unloaded TL, the dispersion starts to resemble a straight line (light line, if $\epsilon_{\text{eff}} = 1$) and the Bloch impedance becomes Z_0.

4.2 Cascade Design

Now, we want to model a finite antenna with some number of unit cells. We cannot use the dispersion diagram anymore as a tool if we want to be exact. The diagram helps only to fix f_0, the pass band and the theoretical leaky-wave (LW) region with help of the light lines. Since the unit cell does not include too many components, it is possible to build an ideal transmission (ABCD) matrix model. The unit cell can be cut from an infinite array of transmission lines, L and C at any place, but let us use the already mentioned symmetric unit cell as in Fig. 9. The ABCD matrix of each element is easy to form just by multiplying the two-port components' ABCD matrices [24]. The calculations are presented in Appendix B to get one ABCD matrix for the whole unit cell. With this unit cell ABCD matrix we can easily analyze 1-D structures with N unit cells in cascade. When using the symmetrical model with two-fold series loading, we can take care of the remaining extra capacitance $2C$ at both ends of the structure in case of many unit cells by multiplying the structure with a series element of $2C$ so that just C remains. This way the realization has only series elements of value C.

Let us choose the second row from Table 1 with $L = 2.00$ nH and $C = 0.80$ pF. We have drawn the dispersion for these values already in Fig. 10(b). The beta-zero frequency is at $f_0 = 2.38$ GHz, and the structure is balanced as seen from the figure. The Bloch impedance is also already presented in Fig. 13(b).

Fig. 14(a) presents the S_{11} and S_{21} parameters for a single unit cell and $N = 9$ unit cells long TLN. $f_0 = 2.38$ GHz can be seen as the second resonance of the single unit cell. The second lower resonance is the resonance frequency of the unloaded TL int terms of L_{TL} and L_{TL}. When we add more and more unit cells next to each other, and remove the two-fold capacitances at both ends, we get more resonances due to the periodic structure familiar from filter design, and we can gradually begin to see the passband from S_{21} of the TLN.

The attenuation and propagation constants for the TLN can be solved from the S_{21} of a finite TLN, and we can calculate the dispersion for finite structures. The propagation constant β is calculated from the phase of S_{21} as

$$\beta = \arctan\left(\frac{\text{Im}\{S_{21}\}}{\text{Re}\{S_{21}\}}\right)\frac{1}{Nd}, \tag{61}$$

where N is the number of cascading unit cells. We have to choose the zero phase shift as a reference at f_0 and then unwrap the periodic phase to get a continuous dispersion curve [6]. The attenuation constant α is calculated from

$$\alpha = \frac{|S_{21}|}{Nd}. \tag{62}$$

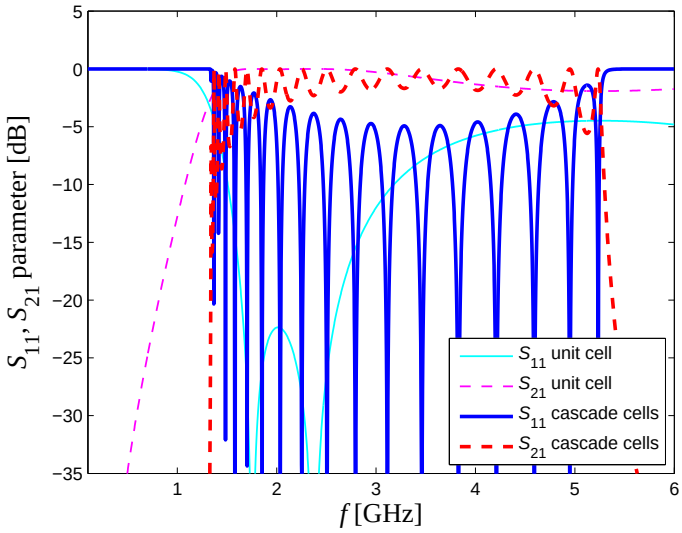

(a)

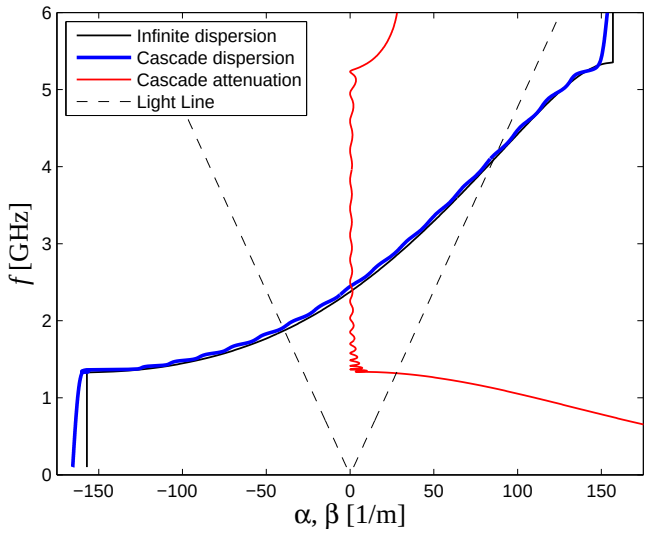

(b)

Figure 14: a) $|S_{11}|^2$ and $|S_{21}|^2$ for the analytical model of one unit cell and $N = 9$ unit cells. b) Analytical propagation and attenuation for $N = 9$ unit cells calculated from S_{21} compared to dispersion of an infinite TLN. Load element values are $L = 2.00$ nH and $C = 0.80$ pF with $f_0 = 2.38$ GHz.

The propagation and attenuation constants for a $N = 9$ unit cells long TLN are shown in Fig. 14(b). Dispersion for an infinite TLN with the same values of L and C is shown as a reference. The finite dispersion curve closes the dispersion of the infinite TLN as N grows, and at $N = 9$ we have a good approximation almost over the whole passband. There is some waviness seen in the dispersion, since S_{21} has also some ripple. If moderate losses are included in this analytical model, the finite dispersion curve quickly becomes smooth.

To verify the results, we simulate the TLN structure with a full-wave electromagnetic simulation software. We chose Ansoft HFSS 10 [2], and built a simple model of the 1-D TLN structure with microstip waveguides and impedance sheets as inductors and capacitors. The series capacitors had now a finite length $l = 2.0$ mm and the transmission lines in HFSS were shortened so that the unit cell length $d = 20$ mm was maintained. The inductors were of course as long as the height h of the substrate. Fig. 15 shows a part of the simulation model. The load values $L = 2.00$ nH and $C = 0.80$ pF are easy to implement in the impedance sheets of the simulation model. TLs were modelled as sheets with zero thickness and PEC boundary conditions, whereas the substrate had the loss tangent $\tan\delta = 0.002$. The ground plane is also PEC and extends the length of one unit cell away from the TLN in every direction. The simulation model had converging problems when a two-port structure was used, so the other end of the TLN was terminated with a vertical impedance sheet with $R = Z_0$.

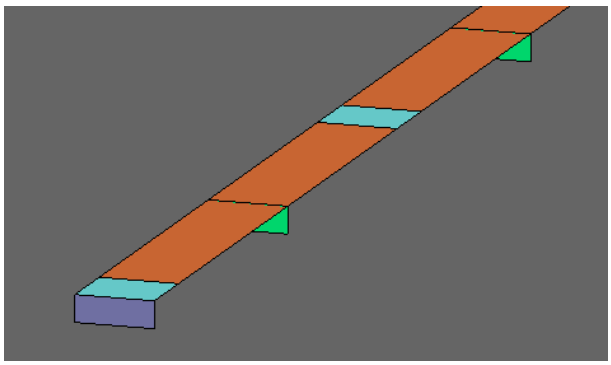

Figure 15: HFSS simulation model. Termination resistance, series capacitances and shunt inductances are modelled as impedance sheets. The transmission lines are PEC conductors with zero-thickness. The substrate is hidden for clarity.

Fig. 16(a) shows the S_{11} plot for analytical and simulated cases. In addition to the small difference in the height of the peaks after f_0 and the pass band's upper boundary frequency, there is a notable bump in S_{11} in the HFSS model around 2.4 GHz. Fig. 16(b) shows the Smith diagram for the HFSS simulations.

It is difficult to say from the figures what causes the bump at the vicinity of f_0. The transmission lines and the load elements should in theory cancel each other at f_0, so the load seen from the input should appear real. The S_{11} curve on the Smith diagram however is rotated and the input impedance is complex at f_0. The bump

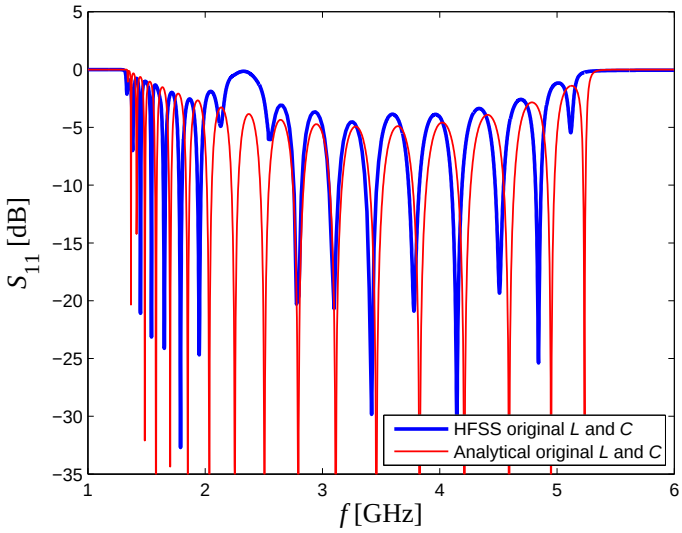

(a)

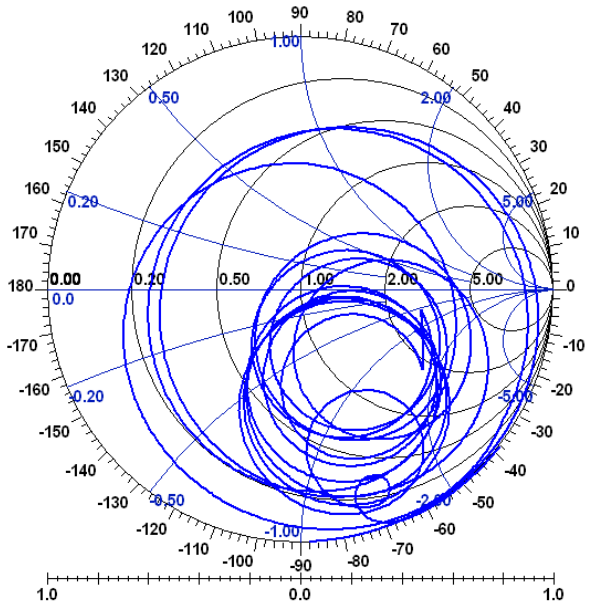

(b)

Figure 16: a) $|S_{11}|^2$ for a 1-D $N = 9$ unit cells long structure calculated with analytical and HFSS model with original values of $L = 2.00$ nH and $C = 0.80$ pF with $f_0 = 2.38$ GHz. b) S_{11} on a Smith diagram for the same structure from HFSS.

could be a rising stop band due to the non-ideal model because the structure is not infinite, nor the loads used infinitesimally short. This was discussed in [44]. So, by tuning the load elements L or C in the HFSS model, it might be possible to remove the bump. This tuning affects both of the propagation constant components α and β. The tuning of the HFSS model should smooth both α and β in the vicinity of f_0.

The unbalanced dispersion can be easily analyzed using the analytical model for the cascade TLN. By tuning the dispersion out from the balanced condition and adding some resistance, we can get a fairly similar S_{11} curve as in Fig. 17, which shows S parameters and input impedance Z_{in} for the $M = 9$ cells long cascade configuration with the inductance $L = 2.35$ nH and capacitance $C = 0.75$ pF in the analytical model. Every unit cell has now the series resistance $R = 0.5\ \Omega$ and the shunt conductance $G = 0.2$ mS, so that we can see real values for Z_{in}. The relation between R and G was chosen using (51) so that $Z_0 = 50\ \Omega$ and the resistive effect is taken into account in both series and parallel resonances equally. The similarities are notable, so it seems that the infinite TLN dispersion can not be used as the only design guideline, at least in the vicinity of f_0.

To verify this assumption, we tuned the HFSS model out from the original values of the infinite dispersion. The new load capacitance value for the *tuned* HFSS model was $C = 0.97$ pF, while the inductance $L = 2.00$ nH was kept the same. Fig. 18 shows the resulting S_{11} values compared to the analytical solution with tuned values for balanced configuration $L = 2.35$ nH, $C = 0.94$ pF, $R = 0.5\ \Omega$ and $G = 0.2$ mS. We see, that the stop band has now almost disappeared from the S_{11} diagram, but the match is not perfect as seen from Z_{in}.

The analytical solution with out-tuned values for nearly same S_{11} suggests that C is approximately corresponding in both the analytical and the HFSS model, whereas $L = 2.00$ nH in HFSS corresponds to a larger L in the analytical model. The difference in the matching can be considerable if theoretical values of L and C are used in HFSS simulations. This has to be kept in mind for future simulations of the 2-D TLN.

4.3 Radiation Properties for the Cascade Design

Since HFSS is a full-wave simulator, it is possible to calculate the far-field radiation even when the radiation mechanism is of a leaky-wave type. The 1-D structure with $N = 9$ unit cells in cascade with $d = 20$ mm is used as an antenna with a feeding point at one end and a termination at the other. The fast-wave, or leaky-wave region can be seen from Fig. 14(b), and it is from $f = 1.9$ GHz to $f = 4.1$ GHz. We then solve the full fields of the HFSS antenna model between these frequencies. From these solutions we can get the complete far-field pattern and the radiation efficiency. We also used the antenna array model of Appendix C as an analytical comparison model. The 1-D array simulations have been done so that the amplitude of the antenna elements have decreased by 10 % at the other edge from the feed, or origin, since the simulated antenna is relatively short. The phase coefficients δ of

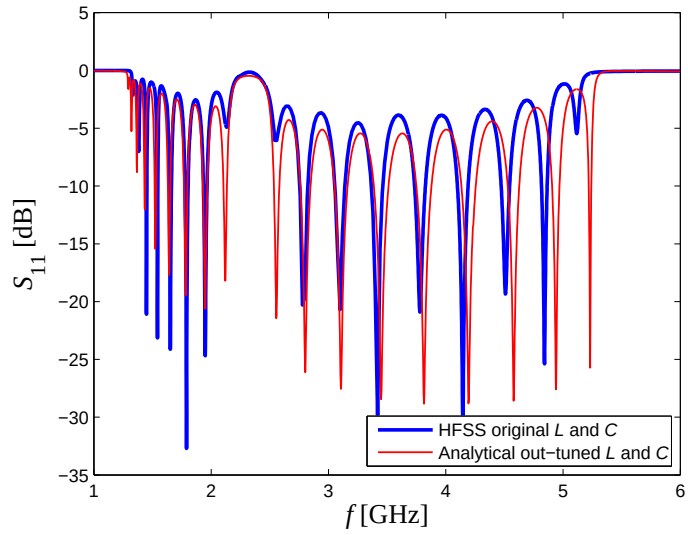

(a)

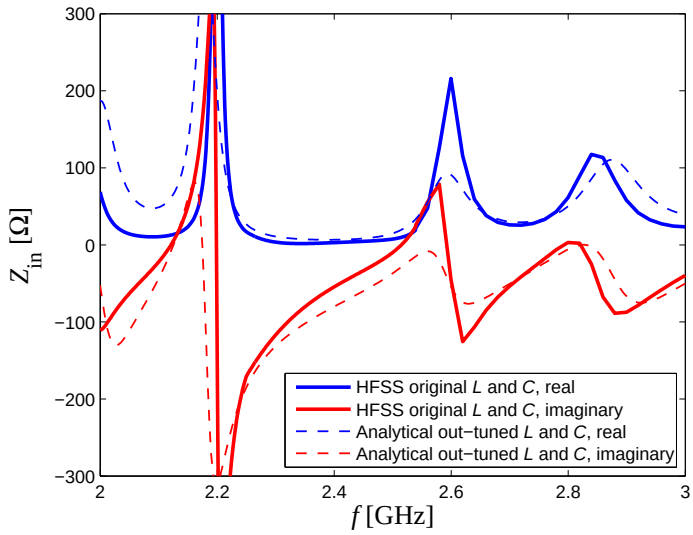

(b)

Figure 17: a) $|S_{11}|^2$ parameter and b) input impedance Z_{in} for HFSS simulation with the original values of L and C and the analytical model with $L = 2.35$ nH and $C = 0.75$ pF, $R = 0.5\ \Omega$ and $G = 0.2$ mS.

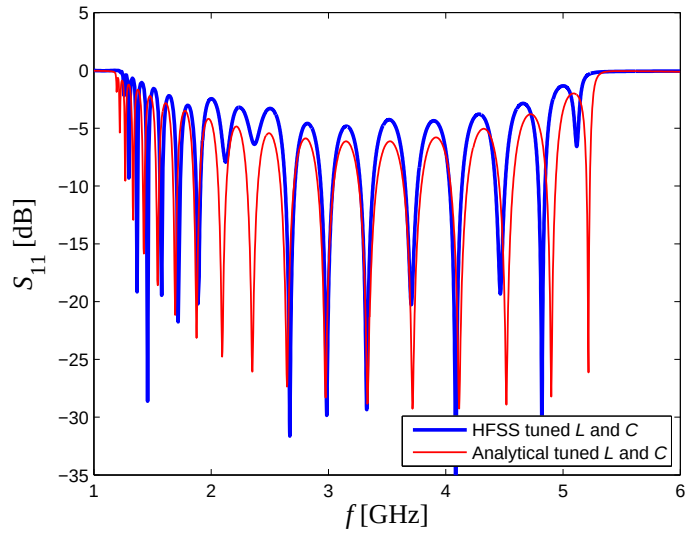

(a)

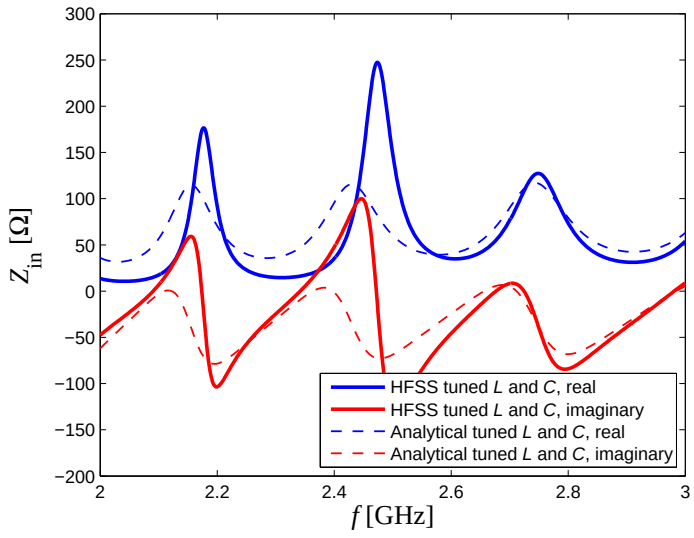

(b)

Figure 18: a) $|S_{11}|^2$ parameter and b) input impedance Z_{in} for HFSS simulation with the tuned values of L and C and the analytical model with $L = 2.35$ nH and $C = 0.95$ pF, $R = 0.5\ \Omega$ and $G = 0.2$ mS.

the antenna elements are calculated from the original and tuned dispersion of the analytical model for the cascade unit cells. Since the effect on radiation properties of the bump in the S_{11} parameter, or unbalance in the dispersion, is unknown, we use both HFSS models in parallel, and compare the results to the analytical calculations with both original and tuned values of L and C.

The radiation angles θ in the scanning plane for the HFSS model with the original values $L = 2.00$ nH and $C = 0.80$ pF are presented in Fig. 19, and compared to the values calculated with the antenna array model with the original load values and to the values from the analytical equation (29). The HFSS model gives for f_0 approximately 2.5 GHz, which is determined from the frequency of broadside radiation. There is more fluctuation in the HFSS angles compared to the analytical angles. The angles from the antenna-array model give also good results. Both the HFSS and the antenna-array model break down in the limits of the scanning region. At low frequencies or negative angles, the angles diverge from the analytical curve, but are still close until the end of the LW region, which is of course told by the analytical curve. At high frequencies both models give rather consistent solution that differ from the analytical solution: the angles do not reach the end-fire radiation but saturate around 70 degrees. The simulations with HFSS and the antenna array model are done with one-degree precision.

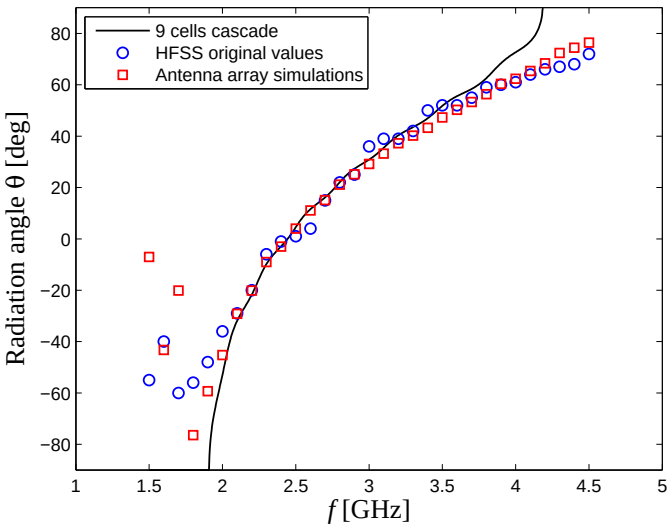

Figure 19: Radiation angles θ from analytical equation with $N = 9$ cascade cells, from the HFSS simulation with the original values for L and C and from the antenna array model.

When we solve the HFSS model's radiation angles with the tuned values $L = 2.00$ nH and $C = 0.97$ pF, we make the comparison to the tuned cascade dispersion. Fig. 20 shows the angles θ for the HFSS and the antenna array model compared to the analytical solution. We note that the behaviour is very similar, with perhaps slightly smoother curve with the angles from the HFSS simulation. Anyway, from this figure

it is hard to tell if there is any real difference to the previous one with the original values of L and C.

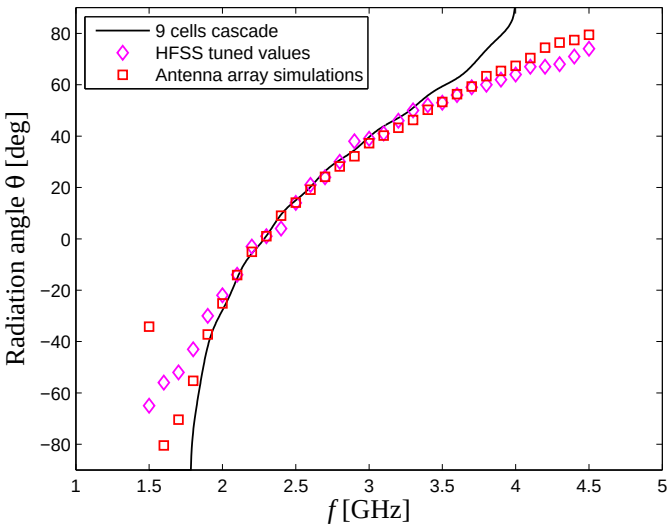

Figure 20: Radiation angles θ from analytical equation with $N = 9$ cascade cells, from the HFSS simulation with tuned values for L and C and from the antenna array model.

Fig. 21 shows the maximum directivities $D_{\max}$ of the HFSS models with original and tuned values of L and C and the antenna array model with the tuned values. Let us first note that the antenna array model does not give reliable directivities compared to the HFSS simulations since the model uses a crude approximation for the unit radiators' far field to simulate the ground effect. Now, we see some difference in the directivity between the HFSS models in the vicinity of f_0, which is about 2.5 GHz for the original model and 2.3 GHz for the tuned. The model with the tuned values seems to have smoother $D_{\max}$ around f_0 than the one with the unbalanced dispersion. The original and tuned HFSS simulations show a slightly increasing directivity over the whole LW region, as does the antenna array calculation.

When we examine the radiation efficiency η_r, the differences in the original and tuned values come more clear. Fig. 22 shows η_r for the HFSS model with the original and tuned values of L and C. We see that overall the efficiency of both of the models is very modest due to the short length of the array. It can also be noted that the efficiency is considerably higher in the original model in the vicinity of f_0. This is explained by the unbalanced dispersion of the finite TLN. It seems that larger attenuation constant is directly seen in the radiation efficiency.

We chose in the beginning of our study to use only L and C components of one value, since this would make the possible realization simpler than with two values. In our 1-D TLN antenna this actually is not the ideal way. If both ends of the TLN would have been left with the double capacitance $2C$, the ripple in the dispersion in Fig. 14(b) would have been absent and matching in Fig. 14(a) better in the lower

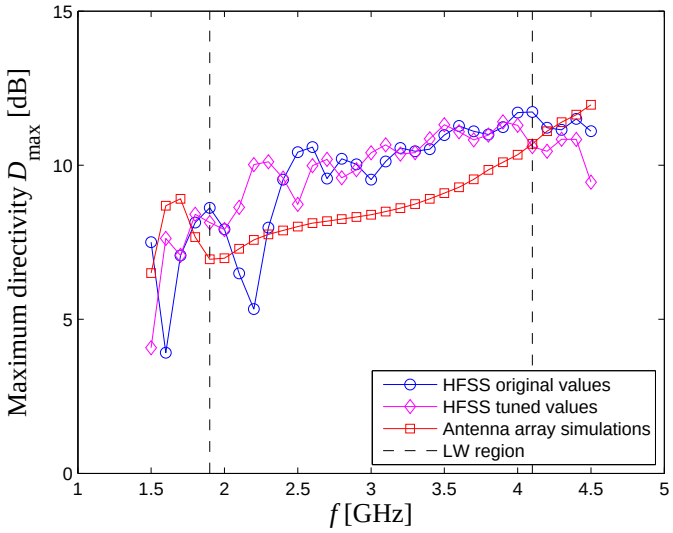

Figure 21: The maximum directivities $D_{\max}$ from HFSS simulations with original and tuned values of L and C. Directivities from the antenna array model are calculated with the original values of L and C. The LW region calculated from the analytical model with cascade unit cells with the original values of L and C is between the dashed lines.

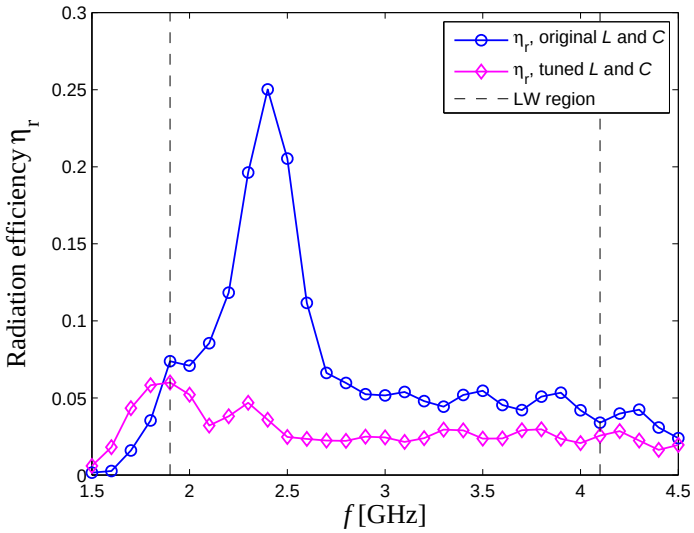

Figure 22: Radiation efficiencies η_r for the $N = 9$ cells long TLN antenna simulated in HFSS with original and tuned values of L and C.

region of the pass band. However, this 1-D antenna is not the goal of our study, so further study with radiation properties has not been done.

The broadside radiation of 1-D periodic LWAs has been recently under study for the conventional $n = -1$ spatial harmonic [45, 46]. These antennas had an open

stop band, that made the broadside radiation impossible with non-zero attenuation constant that seriously affected the radiation characteristics. Later, two different methods for broadside optimization for the 1-D $n = -1$ spatial harmonic LWAs have been proposed by the same group. The first was the U-shaped stub design, which can completely eliminate the open stop band [47]. The second was the combination of a quarter-wave transformer combined with two loading stubs [48]. A third method was also confirmed by the group: the 1-D periodic $n = 0$ spatial harmonic LWA based on loaded transmission lines, or BW TLN [49].

However, even with the BW TLN, the analysis of such structures was seen to be difficult, especially at the frequency of broadside radiation. It was seen, that even if β is relatively smooth, α can still have a noticeably bump, which affects the matching and radiation as we have seen in this section. The solution the group used, was an in-house periodic method of moments code, that was successfully used to solve the attenuation factor for a unit cell. The attenuation factor is the most important parameter next to the phase propagation constant, since it needs to be solved to design a LWA with certain radiation efficiency. Our method of tuning the balanced dispersion with the help of the matching should smoothen the attenuation constant, but we still do not know the absolute value of α, so the analysis is not complete.

5 Design of a 2-D TLN Antenna

The very aim of this study is to determine if a uniformly lit conformal antenna could be designed with the help of loaded transmission-lines networks. Can it be realized without a complex feeding network, with perhaps one simple feed? This we are trying to find out in this section. There is a fundamental problem with a center feed for the TLN antenna because of the destructive interference, if broadside radiation is desired. This leaves only the edges of TLN free for feed points.

5.1 Edge-Fed 2-D Antenna

As mentioned in Section 2.2, a planar antenna with an edge-feed has been designed using Wilkinson power dividers and measured in [23]. The proposed antenna used transmission lines located at one edge of the 4×4 TLN as feed points, while the other edges are matched. The structure was basically designed by arranging 1-D TLNs next to each other, so the functionality was easy to understand. Frequency scanning was measured in the E-plane, and it was argued that such an antenna could be capable of half-space scanning in multiplanes, given a more complicated feeding method, i.e. introducing phasing to the feed ports. We also designed and simulated this kind of edge-fed structure, and found that the edge-feeding indeed works, at least with uniform amplitudes in each port. However, to achieve uniform feed to each microstrip in one edge, power dividers must be used which can easily take as much space as the whole TLN. And worst of all, the number of dividers increases when the unit cell number is increased.

The design procedure for a 2-D TLN is similar to the 1-D case: we can calculate the dispersion for the network with Eq. (57) and plot also the Bloch impedance Z_B. Table 2 shows the values of pass band and Z_B for a 2-D TLN with axial propagation with different values of load elements. This time Z_B does not have any singularity, and the Z_B can be matched to the TLs' characteristic impedance Z_0 with proper choosing of L and C. If we choose the same value for the capacitor C as in the 1-D case, we get the same f_0 with half the inductance L, as seen from Section 3.4. We chose $Z_B = 46.2\ \Omega$, because it is so close to $Z_0 = 50\ \Omega$ and we have proper SMD inductors for possible realization.

Table 2: The values of L, C, f_0, pass band start frequency f_1 and stop frequency f_2, bandwidth Δf and Z_B at f_0 in balanced axial 2-D dispersion for $d = 20$ mm.

L [nH]	C [pF]	f_0 [GHz]	f_1 [GHz]	f_2 [GHz]	Δf [GHz]	Z_B [Ω]
1.0	0.80	2.38	1.55	3.93	2.38	46.2
2.0	1.60	1.76	0.97	3.50	2.53	40.7
2.2	1.76	1.68	0.90	3.44	2.54	40.1
3.3	2.64	1.39	0.65	3.24	2.59	38.5
3.6	2.88	1.34	0.61	3.21	2.60	38.3

5.2 Design of a Corner-Fed TLN Antenna

There are only a limited number of feeding points for a 2-D TLN antenna. As the center feed of the TLN does not seem to work for the broadside radiation, and the uniform edge-fed case has been studied in the literature, only the corner feed needs to be studied. Of course, a more complicated edge feed with changing amplitudes and phases is also possible, but it does not serve our goal of a simple feeding network.

We do not want to have radially spreading voltage waves propagating in opposite directions in the structure, so that no destructive interference can occur. By assuming the waveguides and intersections as ideal line conductors, just like in the circuit theory, we can study the structure. In Fig. 23 the topology of the structure is presented: a 2-D TLN with edges terminated with matching loads Z_0 corresponding to the characteristic impedance of the TLs. If the network is fed from the corner, and assuming that the currents (voltage waves) split equally in the intersections, we see that the combined wave propagates approximately radially from the feed.

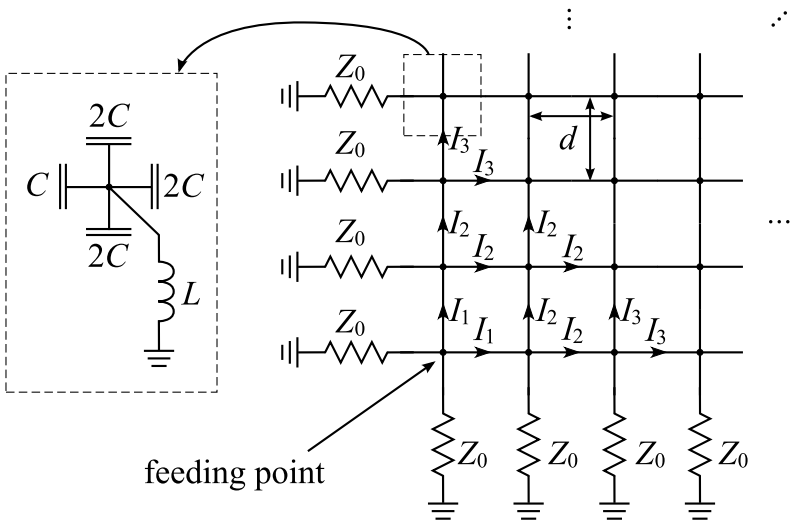

Figure 23: Topology of a 2-D TLN with a corner feed. The unit cell located at one edge has C before the termination, but a unit cell somewhere in the middle of the TLN has $2C$ at every branch.

Now, instead of currents we should talk about voltage waves. Examining the dispersion diagram in Fig. 12 we see that even though $\beta = 0$ at f_0 for all directions, the dispersion in BW and FW regions differ in the axial and diagonal directions. Let us study the axial and diagonal dispersion in the plane more carefully. The loading values for a unit cell with the length $d = 20$ mm are chosen as $C = 0.80$ pF, $L = 1.00$ nH, and the characteristic impedance of the transmission line $Z_0 = 50\ \Omega$. Using these values and inserting them in Eq. (57) we can draw Fig. 24(a), which shows the dispersion in the axial and diagonal directions with $f_0 = 2.38$ GHz. The dashed lines show the LW region between frequencies $f = 2.0 \ldots 3.2$ GHz.

The Bloch impedance is seen in Fig. 24(b) for the axial and diagonal directions in the TLN. We note that the Bloch impedance is also always isotropic at f_0 in case

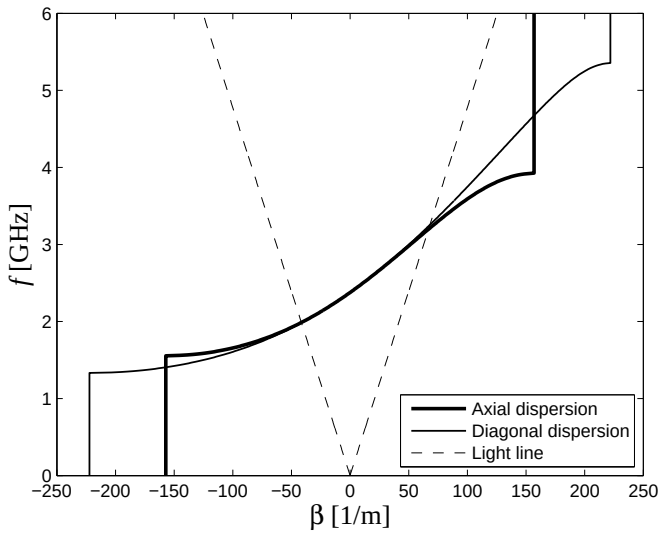

(a)

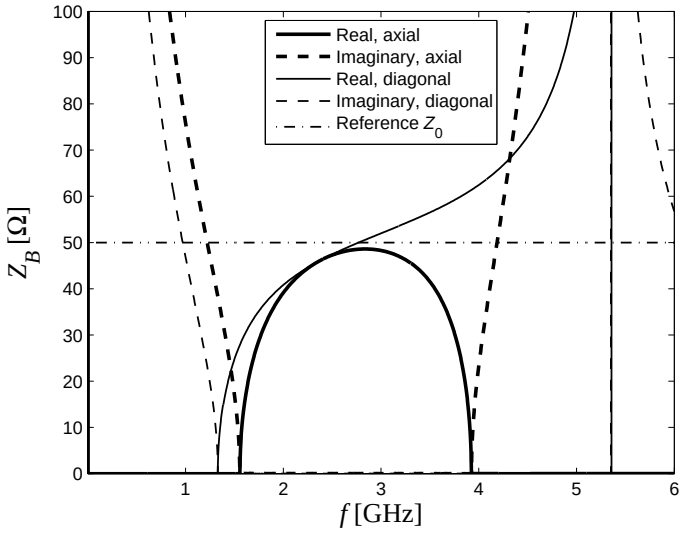

(b)

Figure 24: a) The dispersion and b) the Bloch impedance Z_B for a 2-D TLN in axial and diagonal direction calcualted with $L = 1.00$ nH and $C = 0.80$ pF with $f_0 = 2.38$ GHz.

of balanced dispersion. Table 3 shows the pass band, f_0 and Z_B for a few load element values with balanced dispersion. The diagonal direction has more wide BW and FW regions than the axial direction, so the waves travelling in the diagonal direction experience less phase delay or advance compared to the axial direction. However, in our case this is not problematic, since in the LW region the dispersion is almost the same, as seen in Fig. 24(a).

Table 3: The values of L, C, f_0, pass band start frequency f_1 and stop frequency f_2, bandwidth Δf and Z_B at f_0 in balanced diagonal 2-D dispersion for $d = 20$ mm.

L [nH]	C [pF]	f_0 [GHz]	f_1 [GHz]	f_2 [GHz]	Δf [GHz]	Z_B [Ω]
1.0	0.80	2.38	1.33	5.36	4.03	46.2
2.0	1.60	1.76	0.79	5.36	4.57	40.7
2.2	1.76	1.68	0.73	5.36	4.63	40.1
3.3	2.64	1.39	0.52	5.36	4.84	38.5
3.6	2.88	1.34	0.47	5.36	4.89	38.3

We have also solved the circuit model for the unit cell of a 2-D loaded TLN in the axial and diagonal directions (see again Appendix B). It turns out that the S-parameter behaviour is quite similar to the 1-D case. Fig. 25(a) and Fig. 25(b) show S_{11} and S_{21} for the axial and diagonal propagations, respectively. From the figures we can clearly see the same pass band as seen from the dispersion and the Bloch impedance curve. Also, as apparent from the Appendix, the same two-port model can be used to solve the dispersion and the Bloch impedance for an infinite 2-D loaded TLN as well, so Eq. (57) is needed only for verification.

5.3 Simulations of the Corner-Fed Antenna

Analytical examination of a 2-D corner-fed TLN antenna becomes difficult since we cannot have any specific second port but many terminations. The functionality of the TLN antenna has to be determined afterwards, but we still can study the matching through S_{11}. We use full-wave, circuit and MATLAB simulations. Basically we use a similar circuit model as in Fig. 23. Since we want the power to move away from the corner, we remove the first two branches of $d/2$ long microstrips closest to the feed, and get Fig. 26(a).

Simulations in HFSS are done with a simple model, derived from the 1-D simulations (see Fig. 26(b)). The port is realized as a $Z_0 = 50\ \Omega$ round coaxial cable fed through the ground plane to a junction of intersecting microstrips. The ground plane is again finite so that it extends the length of one unit cell away from the TLN. Simulations in ADS are done with ideal lumped components and lossless transmission lines.

Fig. 27(a) shows S_{11} for a 6×6 TLN simulated in HFSS and ADS with the load values $L = 1.00$ nH and $C = 0.80$ pF and unit cell length $d = 20$ mm. Fig. 27(b) has also the HFSS result on the Smith chart. Results have some similarities: the pass

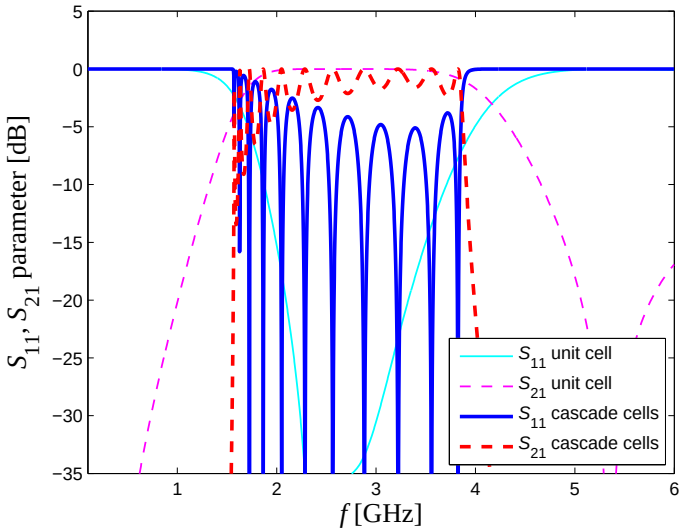

(a)

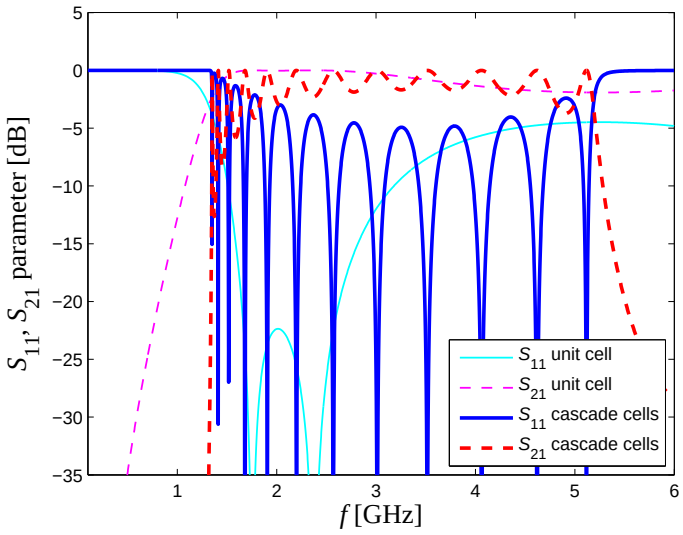

(b)

Figure 25: Scattering parameters for a 2-D unit cell for the propagation in a) axial and b) diagonal direction. Both S_{11} and S_{21} are presented for one unit cell and $N = 6$ cells in cascade.

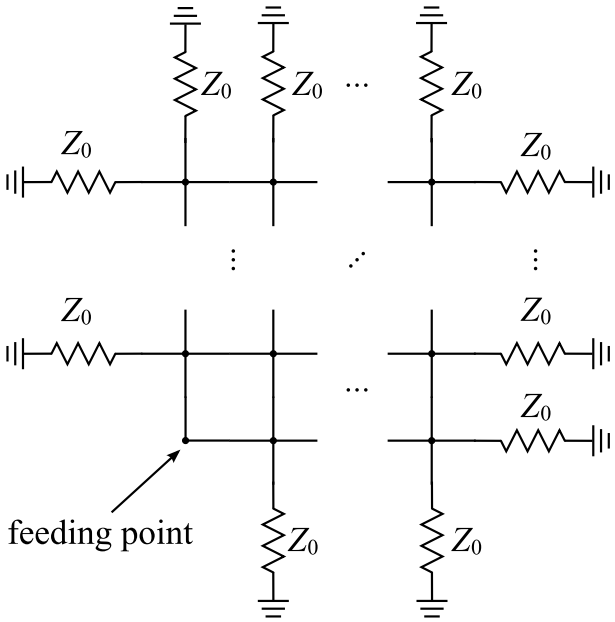

(a)

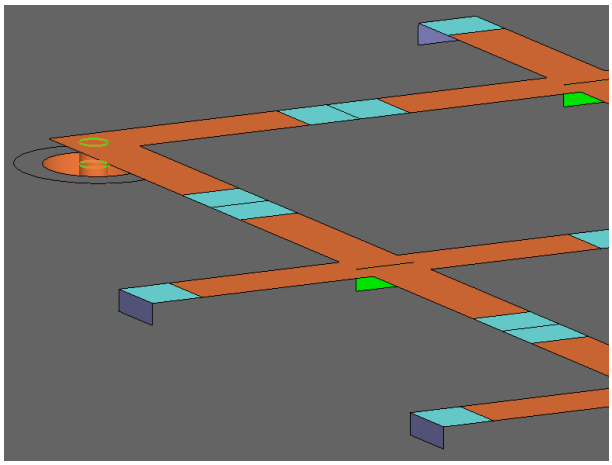

(b)

Figure 26: a) The Modified topology of a 2-D TLN antenna, with the two branches next to the feed point removed. The load elements and TLs hidden for clarity. b) The simulation model in HFSS, with the substrate hidden for clarity.

band is about the same, and near the expected $f_0 = 2.38$ GHz both curves show a mismatch. Above f_0 the simulations have a deeper resonance, but at different frequencies. The matching seems to be very well foreseen from even ideal circuit simulations, and other configurations of TLN with different d and size were studied to confirm this. Also, a similar model than before, but with 4×4 TLN was simulated both in HFSS and ADS, and the results agreed again well.

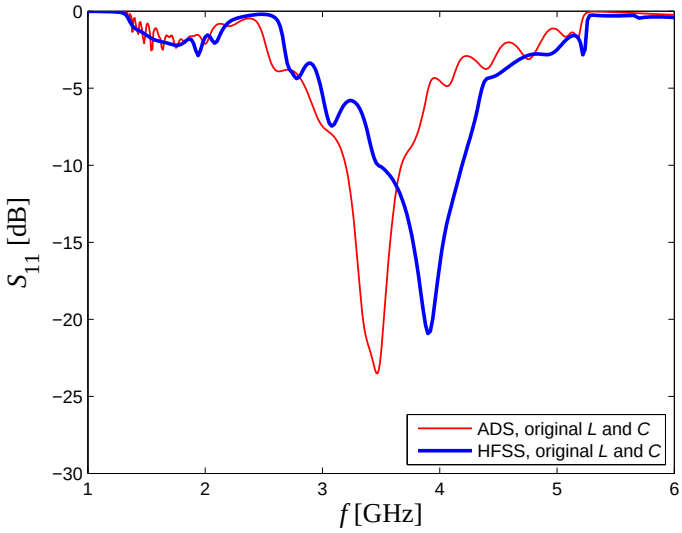

(a)

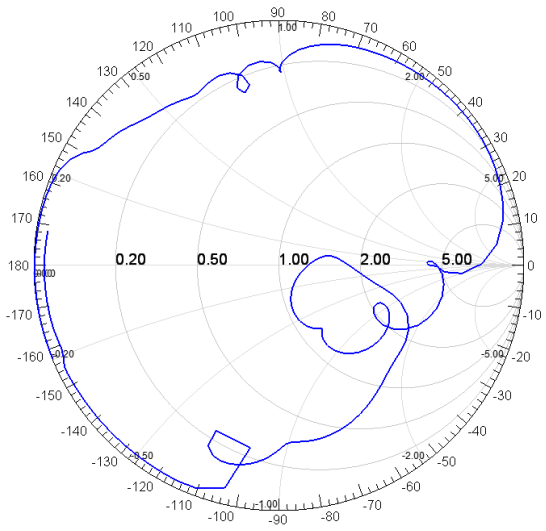

(b)

Figure 27: a) $|S_{11}|^2$ for a corner-fed 2-D 6×6 TLN with $L = 1.00$ nH and $C = 0.80$ pF with $f_0 = 2.38$ GHz calculated with ADS and HFSS. b) S_{11} for a corner-fed 2-D 6×6 TLN on a Smith chart calculated with HFSS.

HFSS simulations are always time consuming, but ADS provides quick simulations for S_{11}. The bump near f_0 does move expectedly when f_0 is changed, which implies

that the root cause is the mismatch in the input impedance seen at the feed, when the load elements L and C and the TL are in resonance, i.e. in balanced dispersion. However, in reference to our previous 1-D simulations, we should also expect a stop band in the vicinity of f_0 for the HFSS simulations. Since these two effects are unfortunately seen in the same frequency region, their segregation is troublesome. One way to balance the HFSS simulation model might be to model a 1-D TLN antenna from 2-D unit cells with HFSS, tune it with the help of the analytical model, and then use these tuned unit cells in the 2-D TLN antenna simulations in HFSS.

This is exactly what was done. We tried to match the HFSS model's S_{11} to that of Fig. 25(a). The simulation model was similar to that in Fig. 15, except that at the locations of every inductance sheet we had TL stubs terminated with a capacitance sheet and the number of cascaded cells was $N = 6$. No terminations were used in the stubs, as no terminations were used in the analytical model of Appendix B. Again, the simulation with the original values showed a stop band in the vicinity of $f_0 = 2.38$ GHz, but after some iteration rounds we saw a curve with no stop band with the tuned value $C = 1.20$ pF, as seen in Fig. 28. One might expect to have the tuned value similar to the 1-D case, but now the simulation model is more complex. The inductance L is now at the crossing of two TL branches, and also the open ended branches have some fringing fields.

Using the analytical model from Appendix B, we calculated S_{11} for $N = 6$ unit cells long 2-D TLN in the axial direction with the balanced values 1.24 nH and $C = 0.99$ pF seen in Fig. 28 resulting in $f_0 = 2.24$ GHz. These values were chosen so that the resulting curves would be close to each other.

Now, using these tuned values $L = 1.00$ nH and $C = 1.20$ pF for the HFSS, we simulated the 6×6 TLN antenna again. S_{11} is seen in Fig. 29 and compared to the ADS model with the new tuned values $L = 1.24$ nH and $C = 0.99$ pF. Now the curves fit better together in the vicinity of $f_0 = 2.24$ GHz, but we still have some kind of a problem with the matching near f_0.

As we have most likely eliminated most of the mismatch due to unbalanced dispersion, the reason for the mismatch lies with the input impedance. The mismatch can be easily understood from the circuit theory. When the loading elements of Fig. 11 are in resonance, they cancel each other, and at the same time the electric length of the transmission lines $\theta = \beta d/2$ goes to zero because $\beta = 0$. This means that the antenna impedance seen from the feed is a huge connection of $Z_0 = 50\ \Omega$ resistors in parallel. The input impedance of this approximation can be easily calculated to be

$$Z_{\text{in}} = \frac{Z_0}{2(2N-1)}, \tag{63}$$

when the branches near the feed are removed. This means that Z_{in} is always very small and real at f_0 for the 2-D TLN with edge terminations. The reader should note that the used HFSS simulation model has the reference plane for the port 15 mm away from the TLN, so the curve on the Smith chart of Fig. 27(b) is rotated clockwise to the upper right quadrant, and f_0 is not anymore on the real axis. This

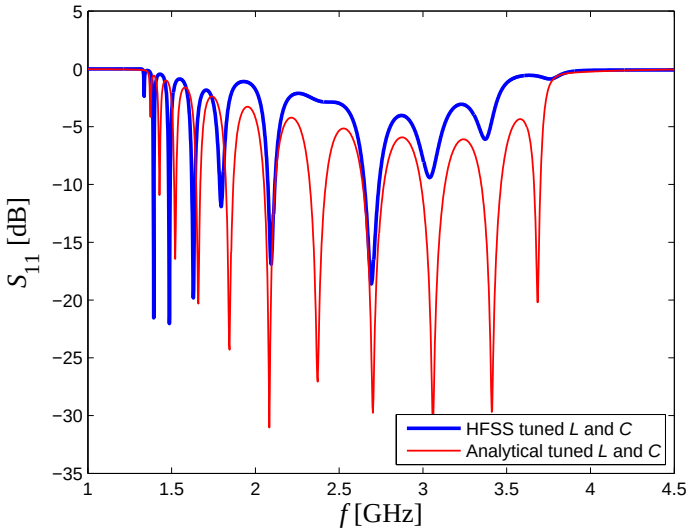

Figure 28: $|S_{11}|^2$ parameter for the axial propagation in the 2-D case with $N = 6$ unit cells in cascade. The tuned values for HFSS are: $L = 1.00$ nH and $C = 1.20$ pF. The analytical model is used for comparison with tuned values $L = 1.24$ nH, $C = 0.99$ pF, $R = 0.5\ \Omega$ and $G = 0.2$ mS.

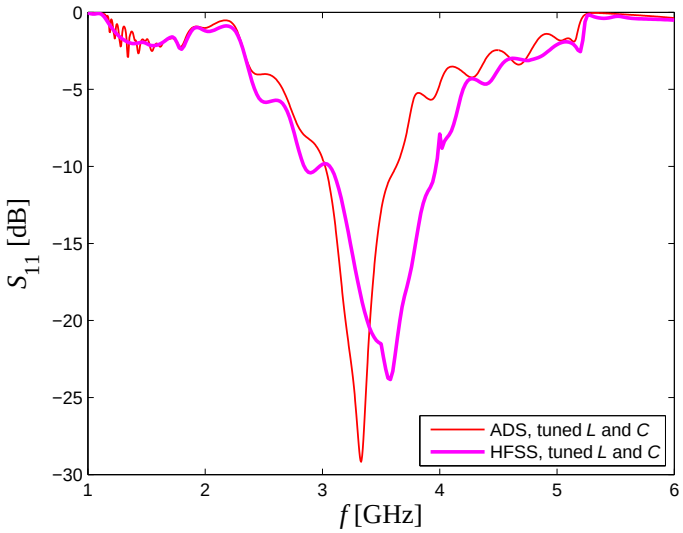

Figure 29: $|S_{11}|^2$ for a corner-fed 2-D 6×6 structure calculated with HFSS with $L = 1.00$ nH and $C = 1.20$ pF and ADS with with $L = 1.24$ nH and $C = 0.99$ pF.

low input impedance is inherent to a TLN with edge terminations at the frequency of zero propagation constant, that cannot be solved using the constant and balanced load values in the unit cells. This means that the same effect is also seen e.g. in the edge-fed 2-D TLN antenna as well.

To verify the wanted behaviour of the propagating waves in the TLN structure, we

study the electric field distributions between the ground and the TLN for the HFSS model with the original load values. We have plotted the real electric field strength snapshots with the chosen phase for the 6×6 TLN with the original load values in all four interesting frequency regions in Appendix D: the BW region at 2.0 GHz, the f_0 point near 2.5 GHz, the FW region at 3.0 GHz and the region with only diagonal propagation at 4.0 GHz. By animating the fields, we can see the direction of wave propagation. As expected, the field propagates according to the theory. At f_0, we do not see any specific propagation, but an evanescent-style wave which attenuates strongly.

In the backward-wave region at $f = 2.0$ GHz the wave front is radial as expected, since the dispersion is nearly isotropic between $f = 1.7 \ldots 3.2$ GHz, and since the phase velocity is directed towards the feed, we can see the electric-field minima seemingly moving also towards the feed. At f_0 around 2.5 GHz we have also similar radial wavefront, but the attenuation is much stronger due to the unbalanced configuration. The forward-wave region at $f = 3.0$ GHz is similar to the BW region, but now we see the propagation away from the feed. When we cross to the stop band of the axial propagation seen from the dispersion diagram in Fig. 24(a) at $f = 4.0$ GHz, the attenuation to those directions grow, and we see clearly a wave beam propagating only in the diagonal direction.

5.4 Radiation Properties of the Corner-Fed Antenna

Now we conduct similar tests for our 2-D 6×6 TLN antenna, than in previous section to the 1-D antenna. We again use both HFSS models with the original and tuned values of L and C. We also use the analytical dispersion, but this time with an infinite TLN, since the propagation direction is no more defined, but can cover all of the directions between the axial and diagonal directions. The antenna array model uses the analytical dispersion for the phase constant, and the amplitude is chosen so, that it has again attenuated by 10 % at the other edge of the TLN.

Fig. 30 shows the radiation angles θ for the HFSS model with the original values $L = 1.00$ nH and $C = 0.80$ pF. They are compared to the angles for the antenna array model and to the angles calculated from the dispersion with Eq. (29). The antenna array model gives good results almost over the whole LW region, as it did in the case of the 1-D antenna. The angles simulated with HFSS however do not match the expected angles very well: the angles do not change as steep as expected. Also, the curve is not very smooth, which may be because of the unbalanced dispersion. The models shows a collapse of directivity, when the planar aperture effect is destroyed at diagonal-only propagation around $f = 4$ GHz, but this is anyway well outside the LW region, and of no practical concern.

When we introduce the tuned values for the HFSS simulation, we see that the curve remains almost the same, as seen in Fig. 31. The curve is at most a little smoother, and of course f_0 is moved accordingly to the load element values. The antenna array model fails to give the correct frequency for the broadside-radiation angle since it

follows the curve for the angles calculated from the analytical dispersion.

However, the antenna array model provides now a better estimate for directivities, as seen from Fig. 32. The figure shows also the maximum directivities $D_{\max}$ for the HFSS models with original and tuned values, while the antenna array model uses the tuned values. Note, that the LW region is now marked according to the analytical dispersion with the original values of L and C. The tuned values give a smoother $D_{\max}$ over the LW region compared to the original values. According to the HFSS simulations, $D_{\max}$ rises near f_0 and then slowly decreases. The antenna array model shows also a rise, but then stays approximately stable.

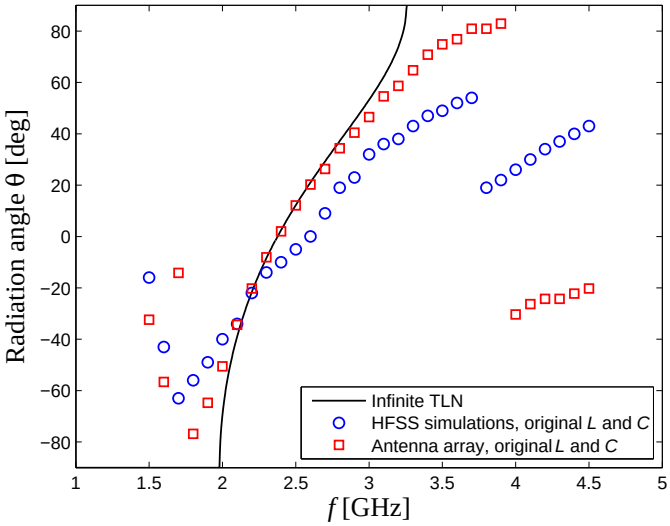

Figure 30: The radiation angles θ using the analytical equation for infinite cascade cells with $f_0 = 2.38$ GHz, the antenna array model and the HFSS simulations of the 6×6 TLN antenna with the original values $L = 1.00$ nH and $C = 0.80$ pF.

We have also calculated the radiation efficiencies η_r for both of the HFSS models. Fig. 33 shows that the η_r for the model with the original values shows again a peak in the vicinity of the expected f_0 because of the unbalanced dispersion. The model with the tuned values shows a smoother curve, so the used values seem to be better in balance. Tuning of the 2-D unit cell's load-element values can be difficult using our method of matching S_{11}. When the realization of the inductance and capacitance is chosen, one may think of simulating just one unit cell by finding the eigensolutions for the fields using a full-wave software, and this way solving the dispersion of the infinite 2-D TLN.

Finally, using the antenna array model, we have estimated the maximum directivities of TLNs of different sizes. Fig. 34 shows the directivities with frequencies corresponding to BW (2.0 GHz), beta-zero (2.38 GHz) and FW (3.0 GHz) regions as a function of the aperture size. The aperture sizes are normalized to our 6×6 TLN antenna. Directivity is proportional to the aperture area, nor to the number of unit cells within it. The figure shows nicely the benefit of the frequency with

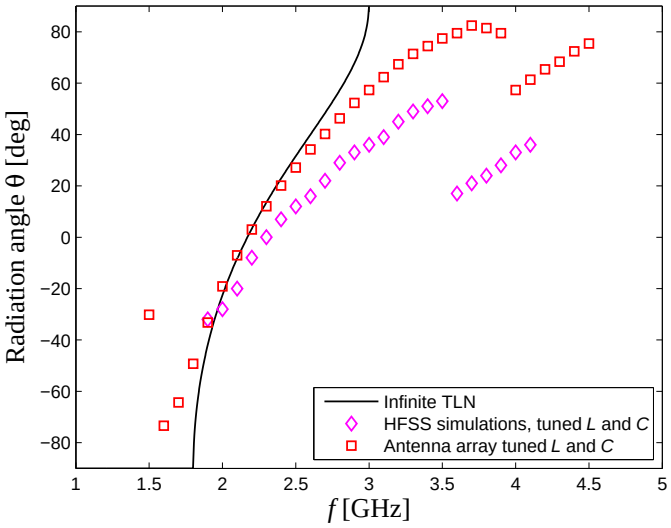

Figure 31: The radiation angles θ using the analytical equation for infinite cascade cells with the tuned values $L = 1.24$ nH and $C = 0.99$ pF with $f_0 = 2.24$ GHz and HFSS simulations with the tuned values $L = 1.00$ nH and $C = 1.20$ pF of the 6×6 TLN antenna.

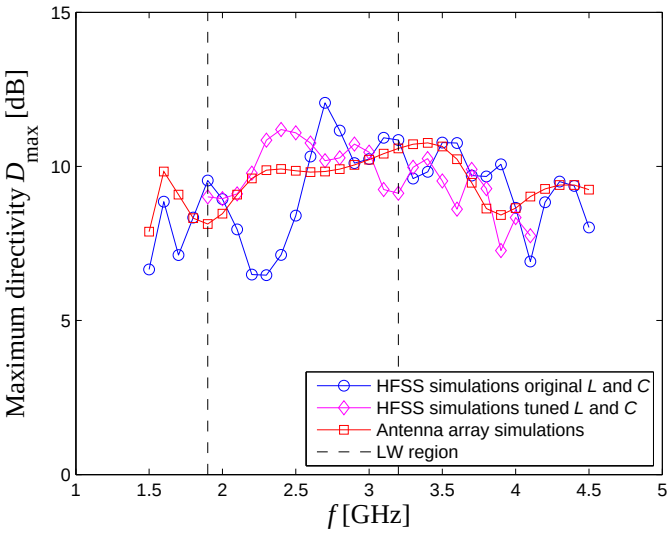

Figure 32: The maximum directivities $D_{\max}$ for the 6×6 TLN antenna. The LW region calculated from analytical dispersion with the original values of L and C is between the dashed lines.

$\beta = 0$, since the directivity increases as the aperture size increases. No destructive interference occurs because of the uniform phase of the antenna elements as opposed to the frequencies with a non-zero propagation constant.

When we consider our goal of a planar 2-D TLN antenna with a simple feed, we

have arrived at an interesting conclusion. The concept of an antenna with a zero propagation constant over the whole aperture is doable, and even frequency-scanning operation is possible. However, when we move from the qualitative model to quantitative realization, we have to introduce some boundaries for our TLN, that seriously harm the matching.

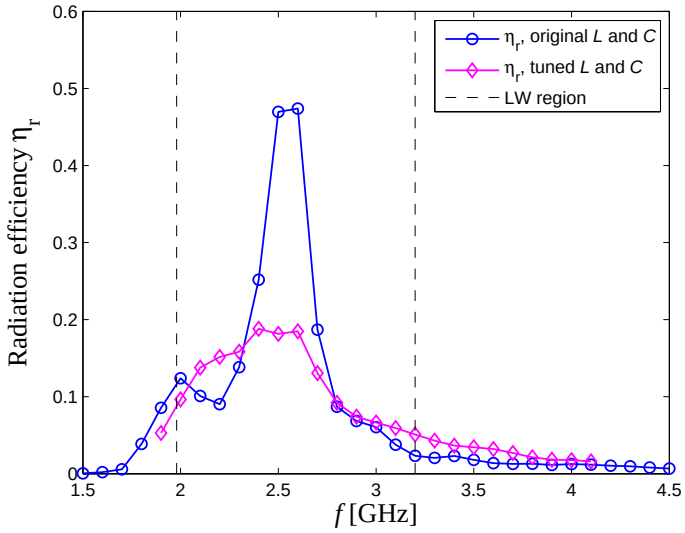

Figure 33: Radiation efficiencies η_r for the 6×6 TLN antenna with the original and the tuned values of L and C. The LW region from infinite dispersion with the original values is between the dashed lines.

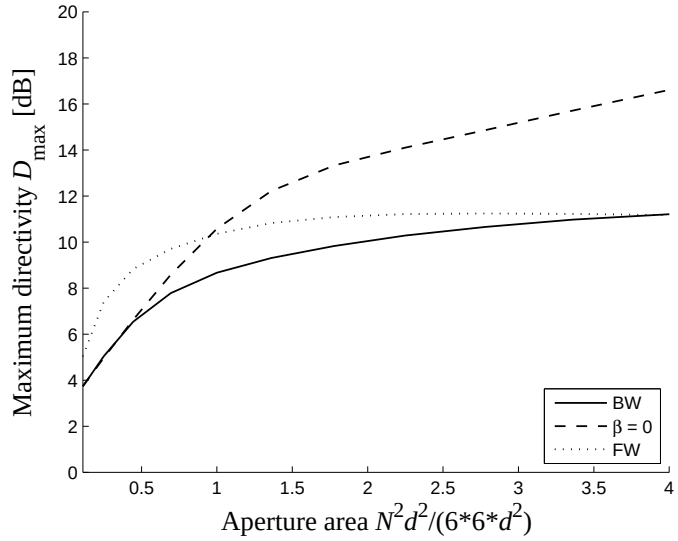

Figure 34: Maximum directivities $D_{\max}$ for a $N \times N$ array at BW (2.0 GHz), f_0 (2.38 GHz) and FW (3.0 GHz) regions as functions of the aperture size normalized to the 6×6 aperture.

5.5 Matched Broadside Corner-Fed Antenna

To make the broadside operation feasible, the corner-fed antenna needs to be matched. We use ADS to design a matching circuit and then use it in the model of the 6×6 TLN antenna with the original values $L = 1.00$ nH and $C = 0.80$ pF. Since the antenna impedance seen at the feed is in the ideal case real, we can use a quarter-wave transmission line to match the antenna. On the other hand, the impedance varies quickly, when we move away from $f_0 = 2.380$ GHz, so we can not expect to have a broadband matching.

The load seen from the feed calculated from Eq. (63) is 2.3 Ω, but we use $Z_{\text{in}} = 1.4\ \Omega$ calculated from ADS. Because ideal matching is not always desired, we do not use the equations for the ideal quarter-wavelength matching circuit [24], but design the circuit with the ADS circuit simulator. If we choose $S_{11} = -6$ dB as the bandwidth limit, the matching at the center-frequency should be close to twice the limit: $S_{11} = -12$ dB [50]. The desired -12 dB matching was achieved with a microstrip with the width $w = 17.0$ mm and the length $l = 15.7$ mm. The TLN antenna was modelled with microstrips of zero thickness, and so is the matching circuit. The frequency response of the quarter-wave transformer is seen in Fig. 35.

The -6 dB band for the matched antenna is seen in Fig. 36 and is from $f_1 = 2.345$ GHz to $f_2 = 2.410$ GHz, resulting a bandwidth of 65 MHz, or 2.7 %. If we compare this band to the radiation directions calculated with the analytical dispersion in Fig. 30, we see that it corresponds to scanning between $\pm 4°$. As the dispersion and the scanning behaviour depends on the unit cell length and the load reactances, the scanning range can be up to some point adjusted by choosing d, L and C differently.

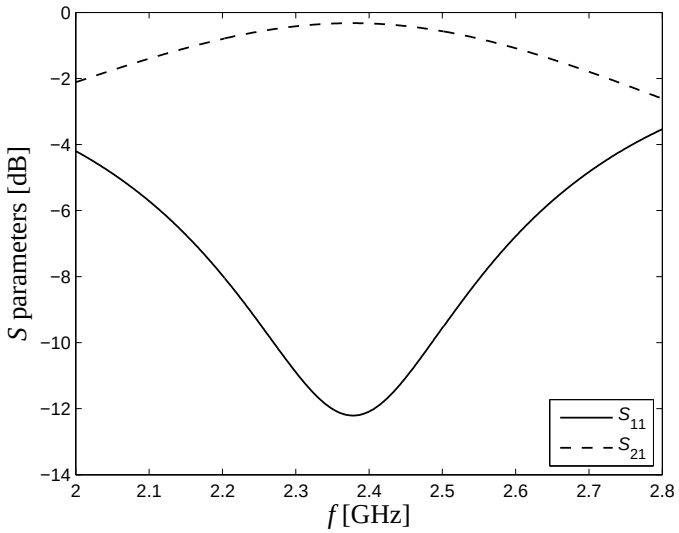

Figure 35: $|S_{11}|^2$ and $|S_{21}|^2$ for the 50 Ω → 1.4 Ω quarter-wave matching circuit simulated with ADS.

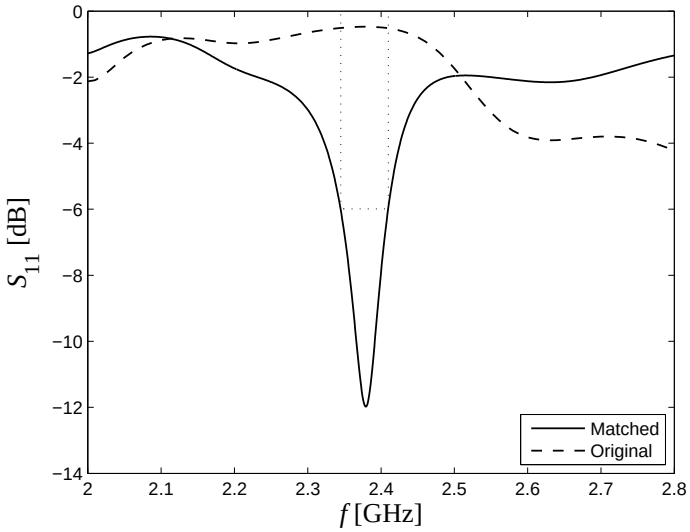

Figure 36: $|S_{11}|^2$ for the corner-fed antenna matched with the quarter-wave matching circuit simulated with ADS. The -6 dB limit is shown with the dotted line.

This matched 6×6 TLN antenna is designed to operate in the vicinity of $f_0 = 2.38$ GHz. The size of the antenna is 120×120 mm^2, or 0.13×0.13 λ_0^2 at its operational frequency. The simulated broadside maximum directivity is $D_{\max} = 11$ dB and the simulated radiation efficiency using impedance sheets is $\eta_r = 0.19$. As in the 1-D case, we know the propagation constant β, but the accurate value of the attenuation constant α is unknown. If α could be accurately solved for some realization of the load values, the antenna size could possibly be calculated for wanted radiation efficiency (usually 90 % or 95 % for LWAs). Of course, the design of the size is now more complicated than for 1-D LWAs, but knowing the exponential decay of the travelling wave, it should be possible.

The main advantage of planar 2-D antennas are clearly their volume. A planar antenna could be attached to walls and other places where volumetrically larger antennas are bulky and unaesthetic. Also, apart from the attractiveness of the size scalability at the frequency of the broadside radiation, the operation frequency can be chosen quite freely by varying the load values and the period of the unit cell.

Frequency scanning using here presented 2-D TLN LWA with a single feed is not feasible. However, frequency scanning is not by any means a necessity, since the proposed matched antenna covers an acceptable bandwidth, and could be thought to work for example as an antenna for IEEE 802.11b/g wireless local area networks with some tuning. Since the operational frequency is not theoretically fixed, the antenna can be used for future radio systems operating at higher frequencies. These kind of radio systems operating for example at 60 GHz are designed for indoors because of strong atmosphere attenuation [51], and thin-sheet antennas may be desired.

6 Conclusion

In this thesis we have studied loaded transmission-line networks in the view of antenna applications. The work consisted of studying 1-D and 2-D antennas based on the fact that the phase of the fields can be made uniform in the TLN by loading the TLN with reactive components. The main goal of the thesis was to inspect the possibility of a single feed for a 2-D planar antennas. A 2-D TLN antenna is however rather complicated structure, so we started to build the ground for the antenna from 1-D TLN.

The antennas were designed first from the viewpoint of the dispersion of an infinite TLN. The 1-D antenna was modelled using a full-wave software directly from the load element values of the dispersion of an infinite structure, but this presented some problems in the finite-sized TLN. For additional help, an analytical two-port model for the unit cell of a 1-D loaded TLN was derived. The model included the possibility to model losses in the unit cells, and since the model was a simple two-port transmission matrix, it was also possible to study the input impedance and the scattering parameters of the finite-sized TLN structure with the wanted number of unit cells in cascade, as well as the dispersion and the Bloch impedance of the infinite structure. The full-wave software presented a non-ideal solution while using the values from the theoretical dispersion. The analytical model was used to tune the parameters of the full-wave model, and it was seen that the radiation properties of the 1-D TLN antenna were better with the tuned model. An antenna array model was developed to study the radiation directions of the 1-D TLN antenna. It was found, that instead of slow full-wave simulations, the developed analytical circuit model with the antenna array model are good substitutes in the design.

Next, the 1-D TLN structure was extended into two dimensions. The feeding schemes for a 2-D TLN antenna were considered, and we came up with the solution that a corner feed is indeed a possible and simple feed method. The full-wave simulations were again used to verify the operation of the designed antennas. An ideal circuit model was constructed for the antenna with a circuit simulator software, and it was used to compare the input impedance of the antenna. The same problems with dispersion of the finite-sized 1-D TLN antenna were seen as in the 1-D case. The analytical two-port model of one unit cell was extended to the second dimension as well, and it was used to tune the values for the full-wave simulations to have again better results for the radiation characteristics. The impedance of the 2-D TLN antenna can be simulated with the circuit simulator, that gives reliable results in the vicinity of the frequency for broadside radiation. The impedance matching of the antenna was however poor, even after the tuned load element values were used, because of the termination resistances. An example matching circuit was designed, that allowed the TLN antenna to be matched with a relative bandwidth of 2.7 % at broadside radiation frequency. This bandwidth corresponded to scanning of $\pm 4^\circ$ across the broadside.

The design of a 2-D TLN antenna with a simple feed was successful, but a problem was seen with the necessary boundaries for the finite-size realization. It was apparent

that the philosophy behind the behaviour of the aperture with constant phase was correct, but the real-life structure presented challenges, that limited the functionality of the antenna somewhat—this was the price to pay for better radiation properties and flexibility concerning the size of the TLN.

References

[1] *ADS 2005A*, Agilent. [Online]. Available: http://eesof.tm.agilent.com/

[2] *HFSS 10*, Ansoft Corporation. [Online]. Available: http://www.ansoft.com/

[3] *MATLAB*, The MathWorks, Inc. [Online]. Available: http://www.mathworks.com/

[4] V. G. Veselago, "The electrodynamics of substances with simultaneously negative values of ϵ and μ," *Soviet Physics Uspekshi*, vol. 10, pp. 509–514, 1968, originally published in Russian in Uspekhi Fizicheskikh Nauk, vol. 92, 1967, pp. 517-526.

[5] S. Tretyakov, *Analytical Modeling in Applied Electromagnetics*. Artech House, 2003.

[6] C. Caloz and T. Itoh, *Electromagnetic Metamaterials, Transmission Line Theory and Microwave Applications*. New Jersey: John Wiley & Sons, inc., 2006.

[7] J. B. Pendry, "Negative refraction makes a perfect lens," *Physical Review Letters*, vol. 85, no. 18, pp. 3966–3969, Oct. 2000.

[8] D. R. Smith and N. Kroll, "Negative refractive index in left-handed materials," *Physical Review Letters*, vol. 85, no. 14, pp. 2933–2936, Oct. 2000.

[9] R. A. Shelby, D. R. Smith, and S. Schultz, "Experimental verifcation of a negative index of refraction," *Science*, vol. 292, no. 77, pp. 77–79, 2001.

[10] A. Sihvola, "Metamaterials in electromagnetics," *Metamaterials*, vol. 1, no. 1, pp. 2–11, 2007.

[11] I. V. Lindell, S. A. Tretyakov, K. I. Nikoskinen, and S. Ilvonen, "BW media – media with negative parameters, capable of supporting backward waves," *Microwave and Optical Technology Letters*, vol. 31, no. 2, pp. 129–133, Oct. 2001.

[12] G. Eleftheriades, A. Iyer, and P. Kremer, "Planar negative refractive index media using periodically L-C loaded transmission lines," *IEEE Transactions on Microwave Theory and Techniques*, vol. 50, no. 12, pp. 2702–2712, Dec. 2002.

[13] A. Grbic and G. Eleftheriades, "Periodic analysis of a 2-D negative refractive index transmission line structure," *IEEE Transactions on Antennas and Propagation*, vol. 51, no. 10, pp. 2604–2611, Oct. 2003.

[14] C. Caloz and T. Itoh, "Transmission line approach of left-handed (LH) materials and microstrip implementation of an artificial LH transmission line," *IEEE Transactions on Antennas and Propagation*, vol. 52, no. 5, pp. 1159–1166, May 2004.

[15] A. Grbic and G. V. Eleftheriades, "An isotropic three-dimensional negative-refractive-index transmission-line metamaterial," *Journal of Applied Physics*, vol. 98, p. 043106, Apr. 2005.

[16] P. Alitalo, S. Maslovski, and S. Tretyakov, "Three-dimensional isotropic perfect lens based on LC-loaded transmission lines," *Journal of Applied Physics*, vol. 99, p. 064912, 2006.

[17] S. Enoch, G. Tayeb, P. Sabouroux, N. Gurin, and P. Vincent, "A metamaterial for directive emission," *Physical Review Letters*, vol. 89, no. 21, p. 213902, Nov. 2002.

[18] A. Grbic and G. Eleftheriades, "A backward-wave antenna based on negative refractive index L-C networks," in *Antennas and Propagation Society International Symposium 2002, IEEE*, vol. 4, Jun. 2002, pp. 340–343.

[19] A. Grbic and G. V. Eleftheriades, "Experimental verification of backward-wave radiation from a negative refractive index metamaterial," *Journal of Applied Physics*, vol. 92, no. 10, pp. 5930–5935, Nov. 2002.

[20] L. Liu, C. Caloz, and T. ltoh, "Dominant mode leaky-wave antenna with backfire-to-endfire scanning capability," *Electronics Letters*, vol. 38, no. 23, pp. 1414–1416, Nov. 2002.

[21] P. Pan, F.-Y. Meng, and Q. Wu, "A composed right/left-handed waveguide with open-ended corrugations for backward-toforward leaky-wave antenna application," *Microwave and Optical Technology Letters*, vol. 50, no. 3, pp. 579–582, Mar. 2008.

[22] A. Sanada, C. Caloz, and T. Itoh, "Characteristics of the composite right/left-handed transmission lines," *IEEE Microwave and Wireless Components Letters*, vol. 14, no. 2, pp. 68–70, Feb. 2004.

[23] C. Allen, K. Leong, and T. Itoh, "Design of a balanced 2D composite right-/left-handed transmission line type continuous scanning leaky-wave antenna," *Microwaves, Antennas & Propagation, IET*, vol. 1, no. 3, pp. 746–750, Jun. 2007.

[24] D. M. Pozar, *Microwave Engineering*, 3rd ed. John Wiley & Sons, inc., 2005.

[25] D. Sievenpiper, L. Zhang, R. Broas, N. Alexopolous, and E. Yablonovitch, "High-impedance electromagnetic surfaces with a forbidden frequency band," *IEEE Transactions on Microwave Theory and Techniques*, vol. 47, no. 11, pp. 2059–2074, Nov. 1999.

[26] C. Allen, C. Caloz, and T. Itoh, "Leaky-waves in a metamaterial-based two-dimensional structure for a conical beam antenna application," in *MTT-S International Microwave Symposium Digest 2004, IEEE*, vol. 1, Jun. 2004, pp. 305–308.

[27] A. Sanada, C. Caloz, and T. Itoh, "Planar distributed structures with negative refractive index," *IEEE Transactions on Microwave Theory and Techniques*, vol. 52, no. 4, pp. 1252–1263, Apr. 2004.

[28] I. V. Lindell and S. Ilvonen, "Waves in a slab of uniaxial BW medium," *Journal of Electromagnetic Waves and Applications*, vol. 16, no. 3, pp. 303–318, 2002.

[29] A. Lai, K. M. K. H. Leong, and T. Itoh, "Infinite wavelength resonant antennas with monopolar radiation pattern based on periodic structures," *IEEE Transactions on Antennas and Propagation*, vol. 55, no. 3, pp. 868–876, Mar. 2007.

[30] J.-H. Park, Y.-H. Ryu, J.-G. Lee, and J.-H. Lee, "Epsilon negative zeroth-order resonator antenna," *IEEE Transactions on Antennas and Propagation*, vol. 55, no. 12, pp. 3710–3712, Dec. 2007.

[31] S. Lim, C. Caloz, and T. Itoh, "Metamaterial-based electronically controlled transmission-line structure as a novel leaky-wave antenna with tunable radiation angle and beamwidth," *IEEE Transactions on Microwave Theory and Techniques*, vol. 52, no. 12, pp. 2678–2690, Dec. 2004.

[32] T. Zhao, T. Zhao, D. Jackson, J. Williams, H.-Y. Yang, and A. Oliner, "2-D periodic leaky-wave antennas-part I: metal patch design," *IEEE Transactions on Antennas and Propagation*, vol. 53, no. 11, pp. 3505–3514, 2005.

[33] T. Zhao, T. Zhao, D. Jackson, and J. Williams, "2-D periodic leaky-wave antennas-part II: slot design," *IEEE Transactions on Antennas and Propagation*, vol. 53, no. 11, pp. 3515–3524, 2005.

[34] G. Lovat, G. Lovat, P. Burghignoli, and D. Jackson, "Fundamental properties and optimization of broadside radiation from uniform leaky-wave antennas," *IEEE Transactions on Antennas and Propagation*, vol. 54, no. 5, pp. 1442–1452, 2006.

[35] R. F. Harrington, *Time-Harmonic Electromagnetic Fields*, ser. IEEE Press Classic Reissue. John Wiley & Sons, inc., 2001.

[36] A. Sihvola and I. Lindell, *Sähkömagneettinen kenttäteoria, 2. Dynaamiset kentät*. Oy Yliopistokustannus University Press Finland, 1996, in Finnish.

[37] I. Lindell, *Aaltojohtoteoria*. Otatieto Oy. University Press Finland Ltd., 1997, in Finnish.

[38] I. Lindell and K. Nikoskinen, *Antenniteoria*. Otatieto, 1995, in Finnish.

[39] E. Kreyszig, *Advanced Engineering Mathemathics*. Wiley, 1998.

[40] A. A. Oliner, *Antenna Engineering Handbook*, 3rd ed. McGraw-Hill, Inc., 1993, ch. Leaky-Wave Antennas, pp. 10–1.

[41] M. Valtonen and J. Virtanen, *Passiiviset suodattimet*. Helsinki University Press, 2004, in Finnish.

[42] P. Alitalo and S. Tretyakov, "Subwavelength resolution with three-dimensional isotropic transmission-line lenses," *Metamaterials*, vol. 1, no. 2, pp. 81–88, Dec. 2007.

[43] P. Baccarelli, S. Paulotto, D. R. Jackson, and A. A. Oliner, "A new Brillouin dispersion diagram for 1-D periodic printed structures," *IEEE Transactions on Microwave Theory and Techniques*, vol. 55, no. 7, pp. 1484–1495, Jul. 2007.

[44] J. Perruisseau-Carrier and A. Skrivervik, "Bloch wave approach to the design of optimally matched non-effective medium composite right/left handed transmission lines," *Microwaves, Antennas & Propagation, IET*, vol. 1, no. 1, pp. 50–55, Feb. 2007.

[45] P. Baccarelli, S. Paulotto, and D. R. Jackson, "Brodside radiation properties of 1D periodic microstrip leaky-wave antennas," in *ICEAA'05, Turin, Italy*, Sep. 2005, pp. 755–758.

[46] P. Burghignoli, P. Burghignoli, G. Lovat, and D. Jackson, "Analysis and optimization of leaky-wave radiation at broadside from a class of 1-d periodic structures," *IEEE Transactions on Antennas and Propagation*, vol. 54, no. 9, pp. 2593–2604, 2006.

[47] S. Paulotto, P. Baccarelli, F. Frezza, and D. R. Jackson, "A microstrip periodic leaky-wave antenna optimization for broadside scanning," in *2007 IEEE AP-S, Honolulu, Hawaii, USA*, Jun. 2007.

[48] ——, "A novel technique to eliminate the open stopband in 1-D periodic printed leaky-wave antennas," in *EuCAP'07, Edinburgh, Scotland*, 2007.

[49] ——, "Full-wave dispersion analysis and broadside optimization for the microstrip CRLH leaky-wave antenna," in *Metamaterials 2007, Rome, Italy*, Oct. 2007, pp. 489–492.

[50] H. Pues and A. Van de Capelle, "An impedance-matching technique for increasing the bandwidth of microstrip antennas," *IEEE Transactions on Antennas and Propagation*, vol. 37, no. 11, pp. 1345–1354, 1989.

[51] P. Smulders, "Exploiting the 60 GHz band for local wireless multimedia access: prospects and future directions," *IEEE Communications Magazine*, vol. 40, no. 1, pp. 140–147, 2002.

[52] C. Caloz and T. Itoh, "Array factor approach of leaky-wave antennas and application to 1-D/2-D composite right/left-handed (CRLH) structures," *IEEE Microwave and Wireless Components Letters*, vol. 14, no. 6, pp. 274–276, Jun. 2004.

Appendix A

Wave Vector for the Beta-Zero Case

When the leaky-wave structure is lossy, we can write for the wave vector above the interface [38]

$$\mathbf{k} = \mathbf{u}_x(\beta - j\alpha) + \mathbf{u}_z\sqrt{k^2 - (\beta - j\alpha)^2}. \tag{A1}$$

Now, we can expand the square root when β is smaller than the other terms by using the Taylor series expansion [39]:

$$f(x) = f(x_0) + f'(x_0)(x - x_0) + \frac{1}{2}f''(x_0)(x - x_0)^2 + \ldots = \sum_{n=0}^{\infty} \frac{f^{(n)}}{n!}(x - x_0)^n, \tag{A2}$$

which is actually the Maclaurin series expansion, when it is developed around $x_0 = 0$. Substituting the square root term of (A1) to (A2), and retaining the first two terms, we get

$$\begin{aligned}
\sqrt{k^2 - (\beta - j\alpha)^2} &\approx \sqrt{k^2 - (-j\alpha)^2} + \frac{\partial}{\partial\beta}\sqrt{k^2 - (\beta - j\alpha)^2}\bigg|_{\beta=0}\beta \\
&= \sqrt{k^2 + \alpha^2} + \frac{1}{2}(k^2 - (\beta - j\alpha)^2)^{-\frac{1}{2}}(-2\beta + j2\alpha)\bigg|_{\beta=0}\beta \\
&= \sqrt{k^2 + \alpha^2} + j\frac{\alpha\beta}{\sqrt{k^2 + \alpha^2}}.
\end{aligned} \tag{A3}$$

Finally, the expression for the wave vector takes the form

$$\mathbf{k} \approx \mathbf{u}_x(\beta - j\alpha) + \mathbf{u}_z\left(\sqrt{k^2 + \alpha^2} + j\frac{\alpha\beta}{\sqrt{k^2 + \alpha^2}}\right). \tag{A4}$$

Appendix B

Circuit Model for a Symmetric Unit Cell

ABCD parameters for a unit cell can be solved easily by multiplying cascade ABCD matrices for individual components. The needed ABCD matrices [24] are for a series impedance Z

$$K_Z = \begin{bmatrix} 1 & Z \\ 0 & 1 \end{bmatrix}, \tag{B1}$$

for a shunt admittance Y

$$K_Y = \begin{bmatrix} 1 & 0 \\ Y & 1 \end{bmatrix} \tag{B2}$$

and for an ideal transmission line with the electric length θ

$$K_{TL} = \begin{bmatrix} \cos\theta & jZ_0 \sin\theta \\ jY_0 \sin\theta & \cos\theta \end{bmatrix}. \tag{B3}$$

A symmetrical unit cell for a 1-D TLN can be calculated from the topology similar than in Fig. 9. After some algebra we get

$$A = \cos^2\theta[1 + ZY] - \sin^2\theta + j\sin\theta\cos\theta[Z_0Y + 2ZY_0], \tag{B4}$$

$$B = \cos^2\theta[2Z + Z^2Y] - \sin^2\theta[2Z + Z^2Y] + j\sin\theta\cos\theta[2Z^2Y_0 + 2Z_0ZY + 2Z_0], \tag{B5}$$

$$C = Y\cos^2\theta + j2Y_0\sin\theta\cos\theta, \tag{B6}$$

$$D = A. \tag{B7}$$

Note, that we have denoted by Z in the above equations as the whole impedance at both ends of the unit cell. The load impedance in a symmetrical unit cell as a part of a TLN is $Z/2$. Also, the electric length θ of a TL has been used to represent the length of a single TL at the both sides of the shunt load.

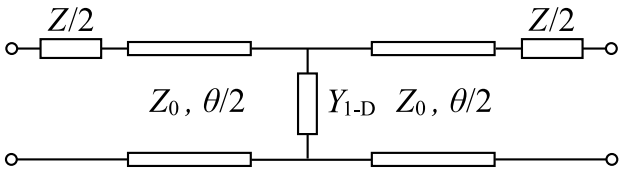

Figure B1: Circuit model for a symmetrical 1-D unit cell.

The ABCD matrix is of course symmetrical ($A = D$) and reciprocal ($AD - BC = 1$), as expected with reactive and passive components. Now, this ABCD matrix can be used to model any number of 1-D TLN unit cells in cascade by inserting for the electric length (see Fig. B1)

$$\theta = \frac{\omega d}{2v_p}, \tag{B8}$$

where d is the unit-cell length and v_p is the phase velocity. For the series impedance we insert

$$Z = \frac{1}{j2\omega C} + \frac{R}{2} \tag{B9}$$

and for the shunt admittance

$$Y = Y_{1-\mathrm{D}} = \frac{1}{j\omega L_{1-\mathrm{D}}} + G, \tag{B10}$$

where $L_{1-\mathrm{D}}$ is the shunt inductance for a 1-D unit cell.

In case of a symmetrical 2-D unit cell, we can easily note that when studying the axial direction, the two orthogonal open-ended stubs form a parallel connection with the shunt admittance of the 2-D TLN $Y_{2-\mathrm{D}}$. So, by transforming the stubs into impedances using [24]

$$Z_{\mathrm{in}} = -jZ_0 \cot(\theta/2), \tag{B11}$$

we get

$$Y_{2-\mathrm{D}} = j\omega L_{2-\mathrm{D}} + G + 2\frac{1}{Z_{\mathrm{in}}} = j\omega L_{2-\mathrm{D}} + j2Y_0 \tan(\theta/2) + G, \tag{B12}$$

because the series impedances at the open ends have no effect if there is no wave propagation through them (see Fig. B2).

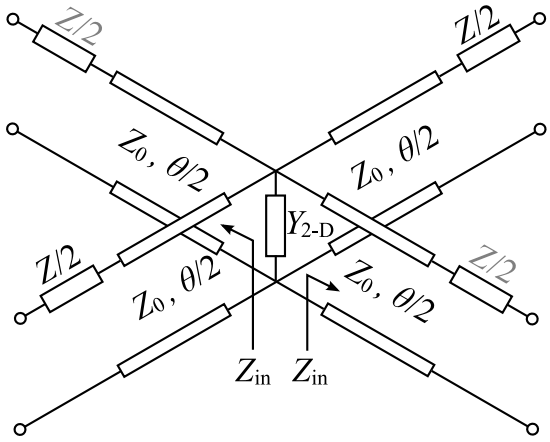

Figure B2: Circuit model for a symmetrical 2-D unit cell for axial propagation.

Next, we derive the circuit model for diagonal-only propagation. Now, in diagonal propagation both branches are equal, so we divide the unit cell into two parts by splitting $Y_{2-\mathrm{D}}$, as in Fig. B3. Transmission lines provide only a phase change, so the two TLs side by side are equivalent to one line. And now we have a circuit model with $Y_{2-\mathrm{D}}/2$ and the same series impedances $Z/2$.

Finally, we see that these models are easily scalable to the third dimension. The axial propagation is the same as in 2-D, except that we have to use the proper shunt admittance for 3-D TLN $Y_{3-\mathrm{D}}$, and instead of two stubs, we use four. 3-D diagonal propagation is the same as in Fig. B3, but we only use $Y_{3-\mathrm{D}}/3$. The diagonal propagation in the 2-D plane of the 3-D structure is similar to the diagonal

propagation in 2-D of Fig. B3: we use the proper $Y_{3-\mathrm{D}}/3$, add two stubs in parallel and then slice the whole structure in half by dividing by two. Table B1 shows the summary of the derived load values Y for the same f_0 when a constant Z is used (see Section 3.4 for further explanation).

We have therefore reduced all but one of the Brillouin diagram's directions into a 1-D two port. Using the Floquet principle as in Section 3.3, we see also that we have accidentally solved the dispersion and the Bloch impedance as well, though only in these discrete directions. When calculating the Bloch impedance for the diagonally directed propagation, the values must be divided by $\sqrt{2}$ (2-D) or $\sqrt{3}$ (3-D) to get congruent results with equations in [16]. This is not apparent, when examining only the ABCD matrix and Eqs. (42) and (44). The equations presented here permit the study of finite numbers of unit cells in cascade through S parameters, and they may be useful in real-life realizations of periodic TLNs.

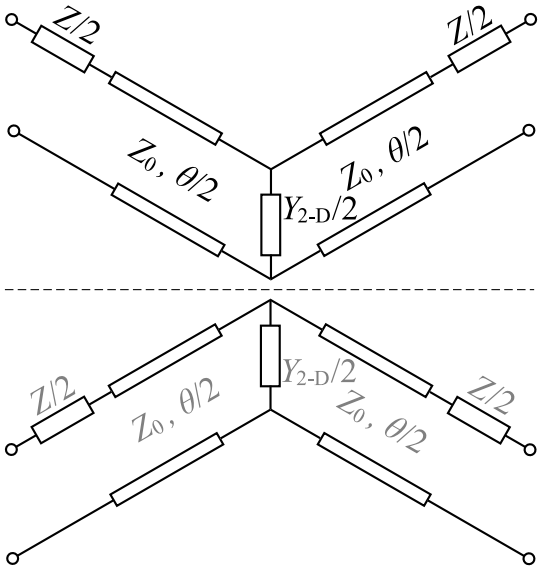

Figure B3: Circuit model for a symmetrical 2-D unit cell with diagonal propagation.

Table B1: Values for Y in 1-D, 2-D and 3-D cases in axial, in-plane diagonal (2-D diagonal) and diagonal (3-D diagonal) propagation directions with constant Z and f_0.

	1-D	2-D	3-D
Shunt Y	$Y_{1-D} = \frac{Z}{Z_0^2}$	$Y_{2-D} = \frac{Z}{2Z_0^2}$	$Y_{3-D} = \frac{Z}{3Z_0^2}$
Axial	Y_{1-D}	$Y_{2-\mathrm{D}} + j2Y_0 \tan(\theta/2)$	$Y_{3-D} + j4Y_0 \tan(\theta/2)$
2-D Diagonal		$\frac{Y_{2-D}}{2}$	$\frac{1}{2}\Big(Y_{3-D} + j2Y_0 \tan(\theta/2)\Big)$
3-D Diagonal			$\frac{Y_{3-D}}{3}$

Appendix C

Antenna Array Model

One way to calculate directivities of complex antennas is the antenna array theory. This has been done successfully to 1-D LWAs with interdigital capacitors and stub inductors [52]. Antenna arrays are based on the assumption that the structure can be divided into smaller similar elementary antennas or elements. From Section 3.2 we know that as long as the antenna element is only moved and the current $\mathbf{J}$ of an element is only multiplied with a complex number, we can find the total array factor AF for the whole structure. Then, if we know the far field of a single element, we can calculate the radiation pattern for the whole structure.

A MATLAB [3] programme was written for calculating the array factors and directivities. We divide the structure first into isotropical antenna elements at distance d from each other. Then we can assign each element a complex number: the magnitude is the amplitude and the imaginary part is the phase of the current element. The amplitude for LWAs is calculated from the relation

$$|\mathbf{J}| \sim |\mathbf{E}| = e^{-\alpha\rho}, \tag{C1}$$

where ρ is the distance from the origin, i.e. from one edge of the TLN antenna. The phase can be calculated from the dispersion, or the phase propagation constant β. If we set the phase to zero at the origin (feed point), we get the phase at each element from

$$\delta = \beta\rho. \tag{C2}$$

Antenna elements were modelled as radiators with cosine function as the radiation pattern so that the maximum radiation was at broadside ($+z$ direction) and zero radiation in $-z$ direction. Fig C1 shows the normalized radiation pattern F of an example array with the cosine function included. The integration for the directivity has been made using the trapezoidal rule in the θ direction of the spherical coordinates and the rectangular rule in the ϕ direction [39]. The antenna array model directivity calculations were verified by calculating the directivity of the Hertz dipole, whose analytical solution is known.

The array factor AF for the 1-D antenna array model with evenly spaced elements is easy to model, since there is rotational symmetry and all the elements 'see' the same elevation angle θ in the far field direction. An antenna array model was also made for the 2-D case to study the directivities of apertures of different sizes. Unfortunately, our 2-D antenna cannot be simply divided into antenna elements, which point into the same direction, as required. However, if we plot the directivity in co- and cross-polarization in HFSS for the 2-D TLN antenna, we see that the polarization is notably pure in the direction of radiation. This means that even though our radiating elements are rotated at different points of the structure, the current components that point in different directions cancel each other. Also, it is possible to realize the radiating elements in such a way, that the currents move

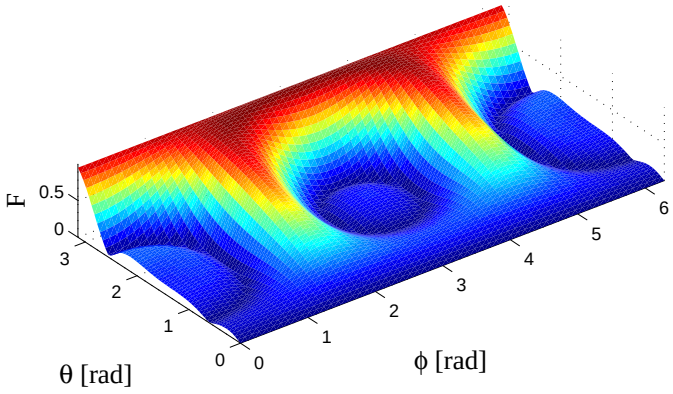

Figure C1: Radiation pattern F example. Notice the cosine-type dependency on the θ coordinate, which simulates the ground plane (here the dependency is actually in the wrong direction, which only means that the $-z$ direction is upwards in the spherical coordinates).

uniformly in the wanted direction. This makes the antenna array approach promising also for the 2-D case. At frequencies where the diagonal propagation is the only allowed propagation, the magnitudes of the 2-D array are set to become zero when the propagation direction closes the axial direction.

The antenna array model can be used to compare the directivities and main beam locations, as done in the text for 1-D and 2-D antennas. We have also calculated radiation patterns of such structures. Figs. C2, C3 and C4 show the radiation patterns F in the scanning plane for $N = 9$ unit cells long 1-D TLN antenna with the tuned loading values $L = 2.35$ nH and $C = 0.94$ pF with the frequencies 2.00 GHz, 2.28 GHz and 3.00 GHz. The frequencies for the main beams somewhat vary for the HFSS modelst from the analytical solution even when using the tuned values, which can be seen from Fig. 19 and Fig. 20. As we can see from the figures, the main beam width of the antenna array model does not exactly match the HFSS model's beam width, so the use of the model is limited. Also, the side lobe levels are quite different as well. There are however some frequencies, where the model predicts the angles of the side lobes, even if not the correct levels.

The above mentioned figures show also the whole radiation patterns in 3-D polar coordinates. Now we can see the plate-shaped radiation pattern, which has transformed into a fan-type pattern because of the cosine type unit radiator. The fan shape, or fan beam, is seen in normal 1-D LWAs. Actually, Fig. C3 shows the 3-D polar-coordinate version of the radiation pattern of Fig. C1. The both long edges wrap to two points: up and down ($+z$ and $-z$), so the pattern is more easily readable.

Figs. C5, C6 and C7 show the radiation patterns in the scanning plane of the 6×6 2-D TLN antenna with original load values $L = 1.00$ pF and $C = 0.80$ pF for $f_0 = 2.38$ GHz. Again, we see some frequency shift due to the difference in dispersion of the analytical solution and the simulated one. This time the main-beam width of the antenna array solution corresponds fairly well to the simulated curve at f_0, but this dependency breaks at other frequencies.

Radiation patterns F are shown in 3-D polar coordinates next to the figures. Here we can see the effect of the 2-D aperture at the broadside frequency: we have a nicely directed and distinctive main beam with relatively low side lobes. According to the antenna array model, higher side lobes actually appear at 45 degrees from the scanning plane, that are not yet seen with a TLN of this small size (about $\lambda \times \lambda$).

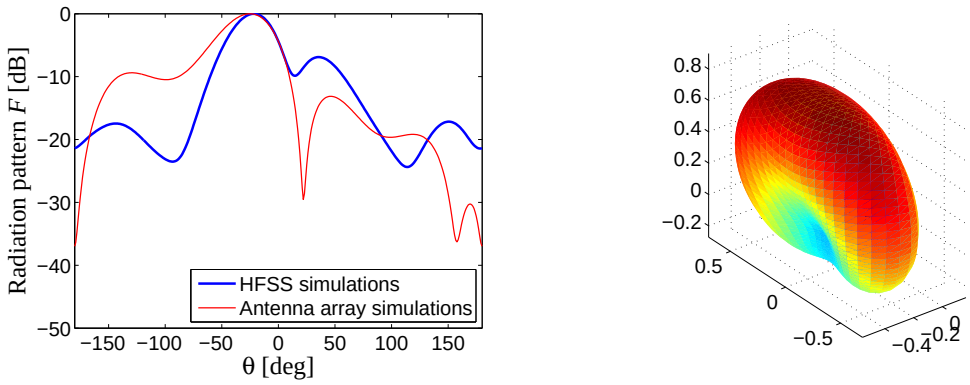

(a) (b)

Figure C2: The $N = 9$ unit cells long 1-D TLN antenna with tuned values and $f = 2.00$ GHz. The radiation pattern F a) in the scanning plane and b) in 3-D polar coordinates.

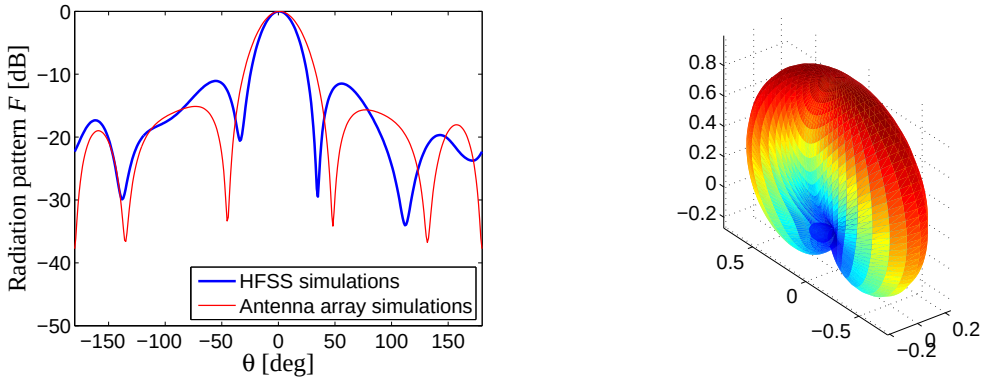

(a) (b)

Figure C3: The tuned $N = 9$ unit cells long 1-D TLN antenna with tuned values and $f = f_0 = 2.28$ GHz. The radiation pattern F a) in the scanning plane and b) in 3-D polar coordinates.

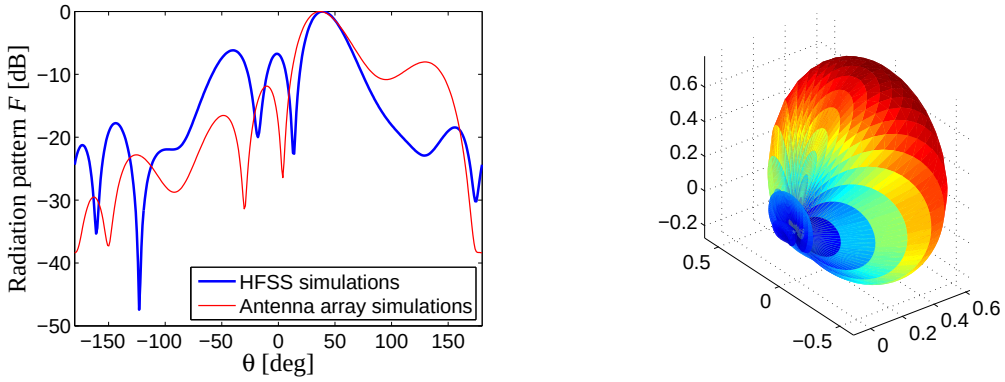

(a) (b)

Figure C4: The tuned $N = 9$ unit cells long 1-D TLN antenna with tuned values and $f = 3.00$ GHz. The radiation pattern F a) in the scanning plane and b) in 3-D polar coordinates.

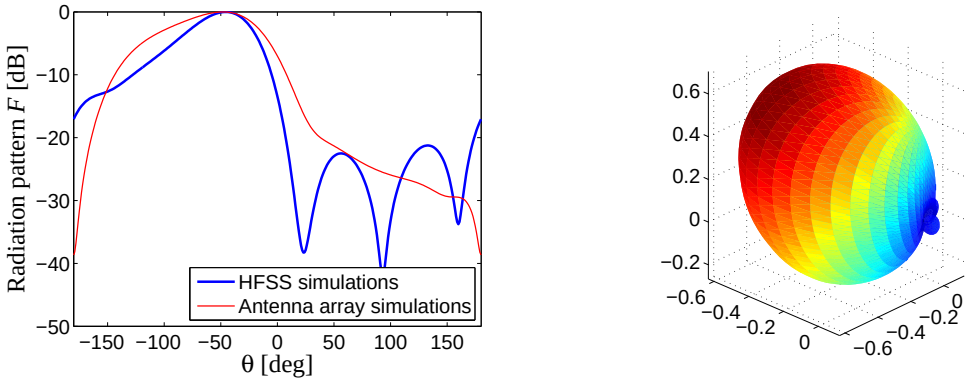

(a) (b)

Figure C5: The 6×6 2-D TLN antenna with original values and $f = 2.00$ GHz. The radiation pattern F a) in the scanning plane and b) in 3-D polar coordinates.

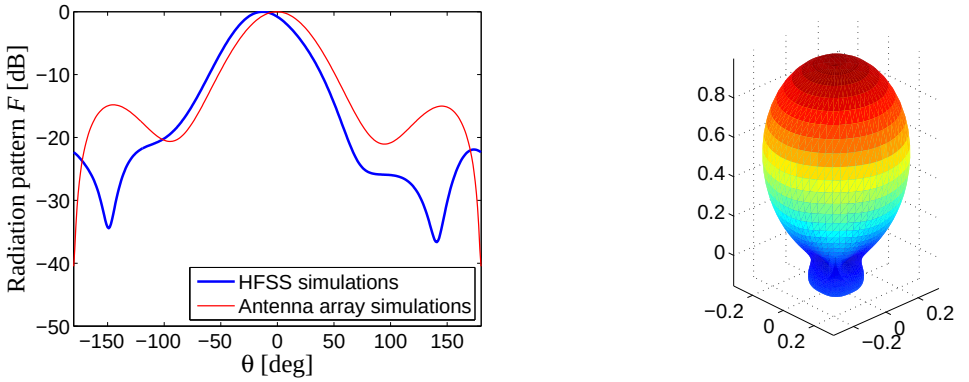

(a) (b)

Figure C6: The 6×6 2-D TLN antenna with original values and $f = f_0 = 2.38$ GHz. RThe radiation pattern F a) in the scanning plane and b) in 3-D polar coordinates.

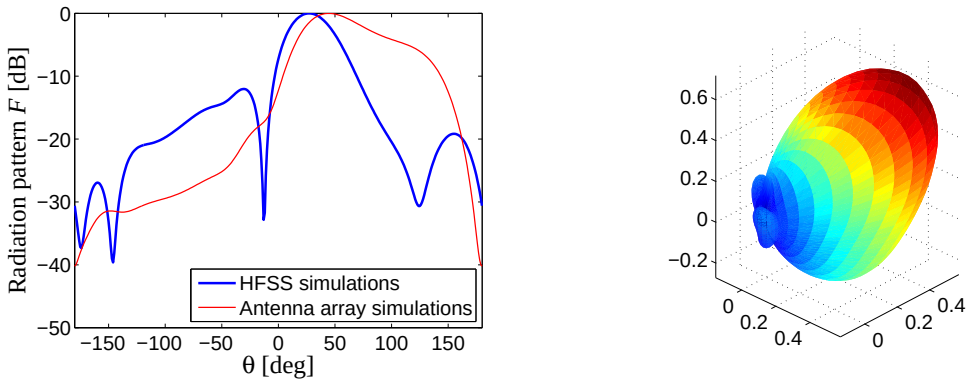

(a) (b)

Figure C7: The 6×6 2-D TLN antenna with original values and $f = 3.00$ GHz. The radiation pattern F a) in the scanning plane and b) in 3-D polar coordinates.

Appendix D

Additional Plots for the 2-D TLN

A 6×6 TLN antenna from Section 5.3 with a coaxial probe feed in one corner was simulated with HFSS. The TLN had the load values $L = 1.00$ nH and $C = 0.80$ pF. The electric field strength between the ground plane and the TLN is plotted for the TLN antenna at frequencies $f = 2.0$ GHz (BW region), $f = 2.5$ GHz (f_0 region), $f = 3.0$ GHz (FW region) and $f = 4.0$ GHz (FW region). The fields are snapshots at some phase chosen for clarity of the real part of the electric field, so we can see the wavefronts with zero field.

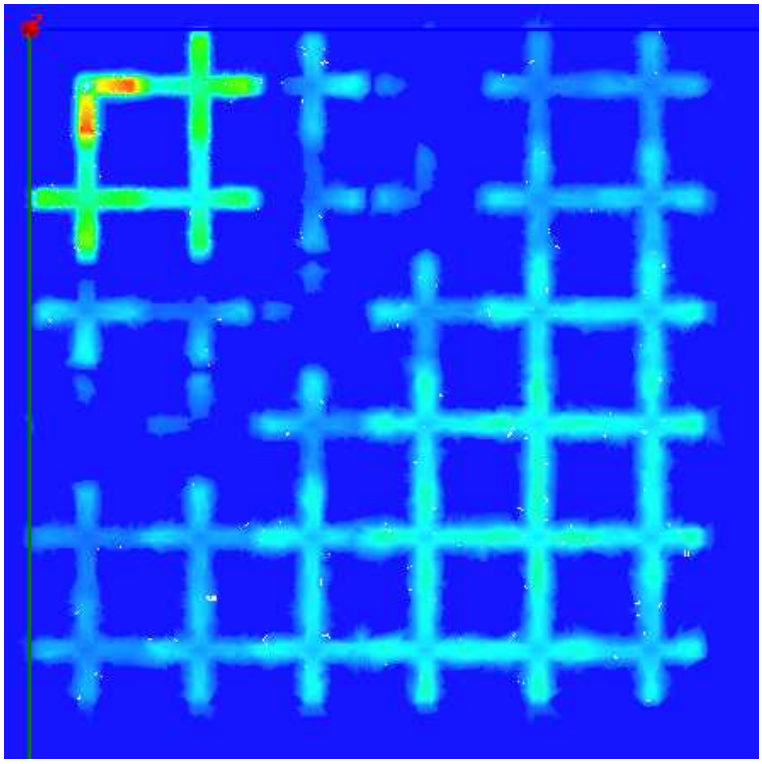

Figure D1: Re$\{\mathbf{E}\}$ plotted in the mid-plane between the ground and the TLN for the 6×6 TLN at $f = 2.0$ GHz.

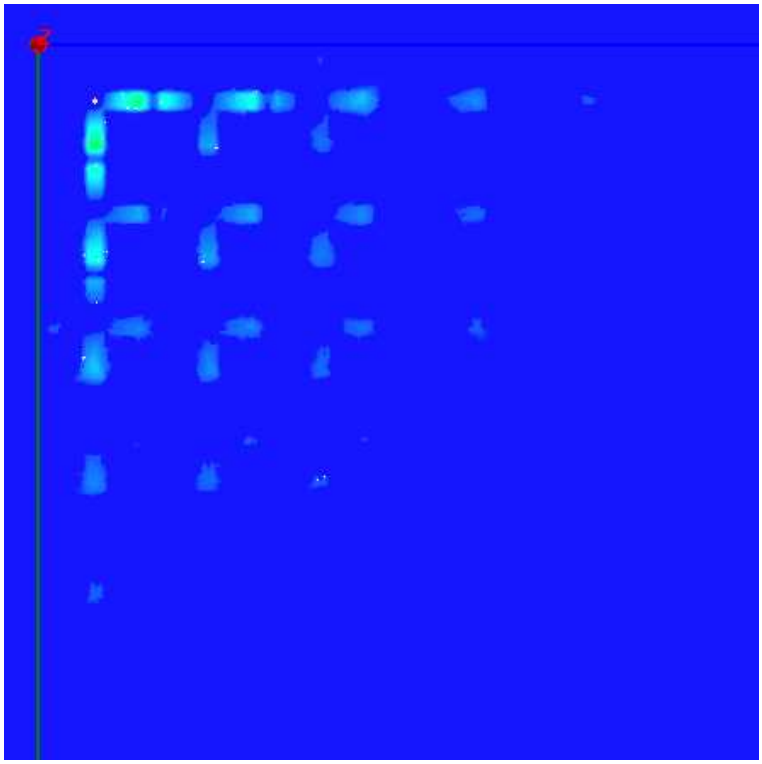

Figure D2: Re{**E**} plotted in the mid-plane between the ground and the TLN for the 6×6 TLN at $f = 2.5$ GHz.

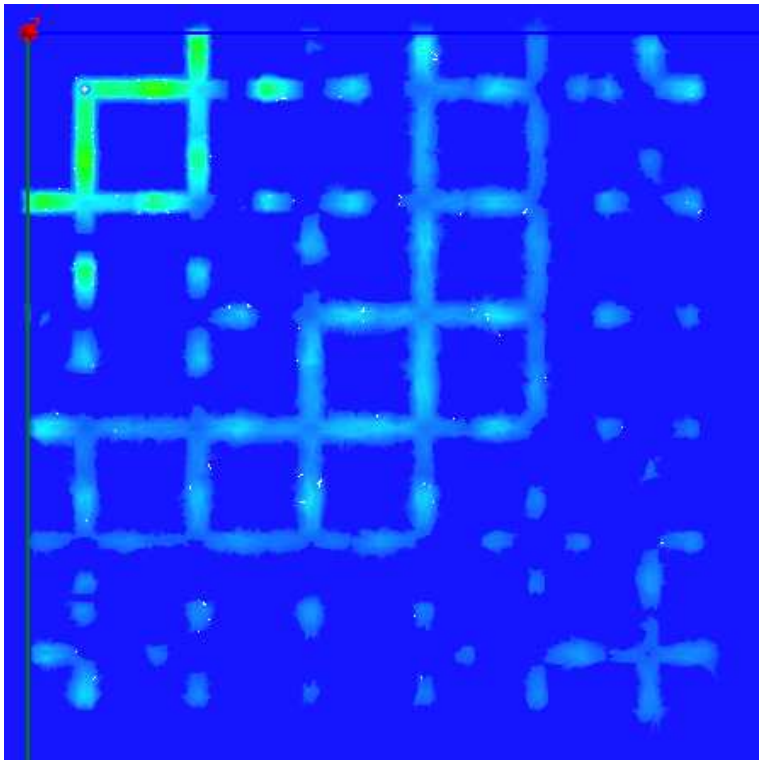

Figure D3: Re{**E**} plotted in the mid-plane between the ground and the TLN for the 6×6 TLN at $f = 3.0$ GHz.

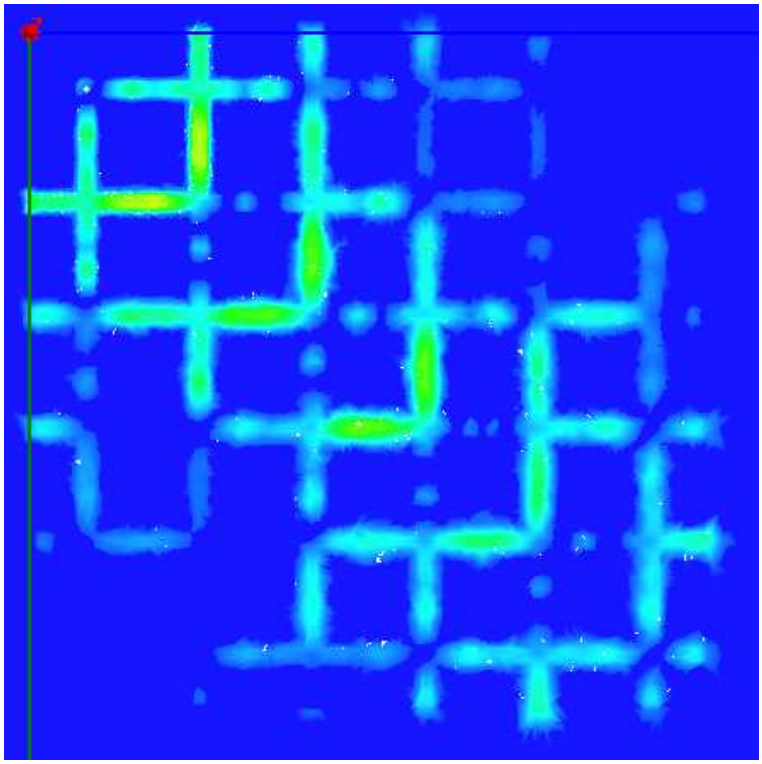

Figure D4: Re{**E**} plotted in the mid-plane between the ground and the TLN for the 6×6 TLN at $f = 4.0$ GHz.